



Lipoic acid-boronophenylalanine-derived multifunctional vesicles for cancer chemoradiotherapy

Received: 6 June 2024

Liqun Dai¹, Jie Liu¹, Tingyu Yang¹, Xiaorui Yu², Yi Lu¹, Lili Pan³, Siming Zhou¹,
Diyun Shu², Yuanhao Liu^{2,4}, Wuyu Mao^{1,5}✉ & Zhiyong Qian¹✉

Accepted: 17 January 2025

Published online: 04 February 2025

Check for updates

Cancer remains a major health challenge, with the effectiveness of chemotherapy often limited by its lack of specificity and systemic toxicity. Nanotechnology, particularly in targeted drug delivery, has emerged as a key innovation to address these limitations. This study introduces lipoic acid-boronophenylalanine (LA-BPA) derivatives that incorporate short-chain polyethylene glycol (PEG) as a spacer. These derivatives distinctively self-assemble into vesicles under specific pH conditions, exhibiting a pH-dependent reversible assembly characteristic. Notably, these vesicles target cancer cells by binding to sialic acid via phenylboronic acid groups, subsequently depleting cellular glutathione and elevating reactive oxygen species, thereby inducing apoptosis via mitochondrial dysfunction and mitophagy. The vesicles demonstrate high efficiency in encapsulating doxorubicin, featuring a glutathione-responsive release mechanism, which present a promising option for tumor therapy. Additionally, the derivatives of the B-10 isotope, containing up to 1.6% boron, are engineered for incorporation into $\text{L}^{\text{p}}\text{B}-3$ -based vesicles. This design facilitates their application in boron neutron capture therapy (BNCT) alongside chemotherapy for the treatment of pancreatic cancer. Our findings highlight the potential of LA-BPA derivatives in developing more precise, effective, and less detrimental chemoradiotherapy approaches, marking an advancement in nanomedicine for cancer treatment.

Cancer remains a formidable challenge to public health, with chemotherapy serving as the most commonly used treatment. Currently, more than fifty FDA-approved antitumor agents are in clinical use^{1,2}. However, these chemotherapeutic agents generally suffer from a lack of selectivity and optimal pharmacokinetics, and their broad mechanisms of action often lead to severe systemic toxicity³. The emergence of nanotechnology has redirected the focus toward drug

delivery methods that aim to mitigate the adverse side effects of chemotherapy, showing promising results in both clinical trials and practical applications. Various nanocarriers, including inorganic nanoparticles, polymers, and lipid-based systems, have been effectively employed to target and deliver antitumor drugs directly to tumor sites. These nanocarriers are capable of transporting diverse drugs, thereby enhancing their efficacy while reducing systemic

¹Department of Biotherapy, Cancer Center and State Key Laboratory of Biotherapy, West China Hospital, Sichuan University, Chengdu 610041, China.

²Neuboron Medtech Ltd., Nanjing, Jiangsu Province, China. ³Department of Nuclear Medicine, Laboratory of Clinical Nuclear Medicine, West China Hospital, Sichuan University, Chengdu 610041 Sichuan, China. ⁴Nanjing University of Aeronautics and Astronautics, Nanjing, Jiangsu Province, China. ⁵Department of Respiratory and Critical Care Medicine, Targeted Tracer Research and Development Laboratory, Institute of Respiratory Health, State Key Laboratory of Respiratory Health and Multimorbidity, West China Hospital, Sichuan University, Chengdu 610041, China. ✉e-mail: wuyanmao1@sina.com

zhiyongqian@scu.edu.cn

toxicity. This approach is further supported by the enhanced permeability and retention (EPR) effect⁴, highlighting the potential for nanomedicines to accumulate more extensively in tumors by extravasating through their fenestrated vessels.

Despite these advancements, only a few nanocarriers have advanced to clinical use for tumor diagnosis and therapy⁵. Ideally, newly developed nanocarriers should deliver drugs specifically to tumor sites while minimizing off-target delivery. Notably, hypersialylation plays a crucial role in tumor growth, invasion, migration, and chemoresistance. Therefore, targeting sialylation regulators such as sialic acid and neuraminidase offers a promising strategy for drug delivery^{6,7}. For example, phenylboronic acid-functionalized nanomaterials have been engineered to enhance tumor targeting and transcellular transfer. This enhancement results from the rapid reaction between the phenylboronic acid group and sialic acid on cancer cells⁸. Moreover, the disulfide bond represents a dynamic, highly controllable, and reversible covalent bond type⁹⁻¹⁴. Previous work has demonstrated that disulfide bonds can act as proton acceptors, being

protonated by acids to form sulfonium cations¹⁵. This reaction efficiently initiates the ring-opening polymerization (ROP) of 1,2-dithiolanes, involving repeated breaking and forming of disulfide bonds until a thermodynamically stable product forms. Disulfide linkers have thus been widely explored in gels^{13,15,16}, elastomers¹⁷, vesicles¹⁸, and recyclable materials¹⁹.

In this work, we describe the design and synthesis of lipoic acid-boronophenylalanine (LA-BPA) derivatives linked by short-chain PEG spacers. These derivatives can reversibly self-assemble to form versatile vesicles under specific pH conditions, making them suitable for applications in cancer therapy (Fig. 1). As known and understood, the nanoparticles would reach the tumor site via EPR effect and accumulated in tumor tissue. To increase the tumor-targeting efficiency, various modifications to nanoparticle have proven to be effective. Based on the affinity of phenylboronic acid group to the sialic acids on the tumor cells, the cell-vesicles interactions were greatly increased, and more vesicles were associated with the cell's surface, which would facilitate the entrance of the L^PB-3 vesicles into cells. Under acidic

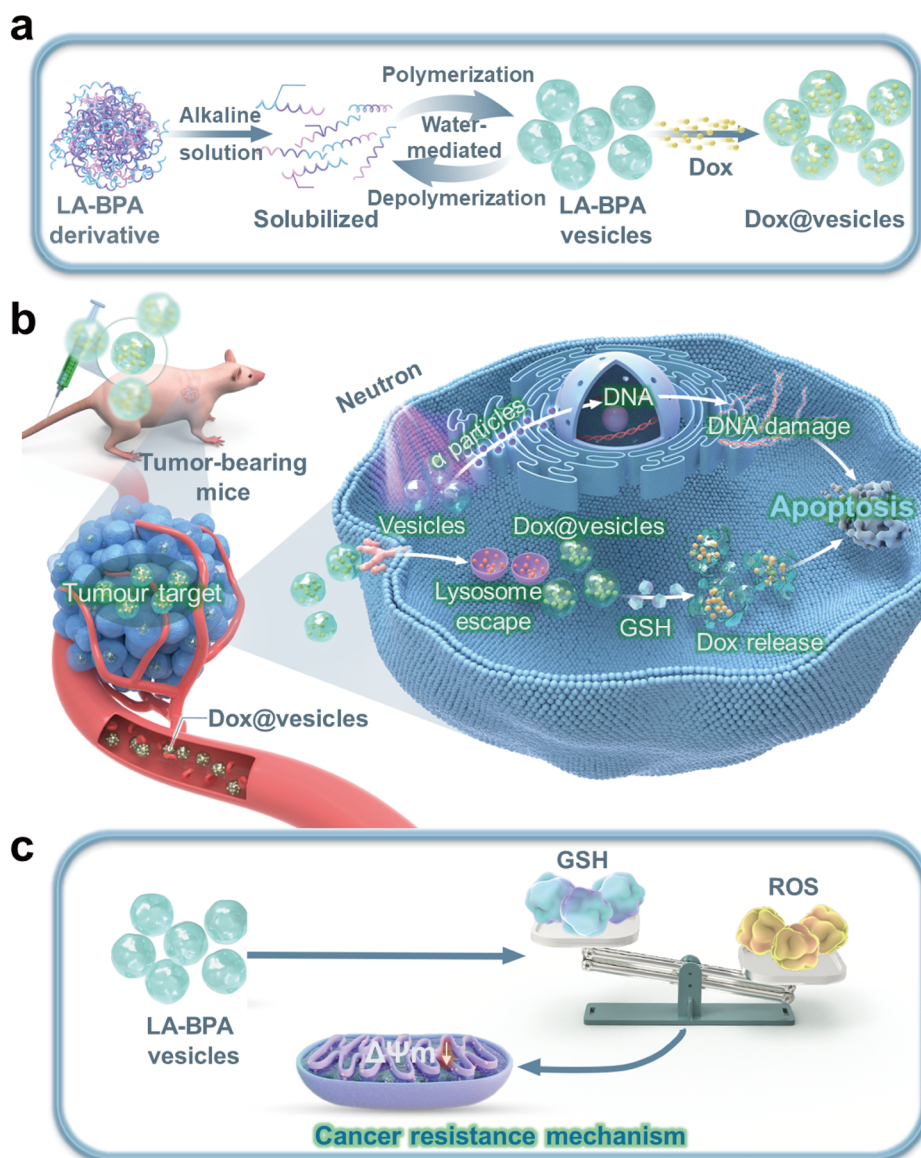


Fig. 1 | Schematic illustration of lipoic acid-boronophenylalanine derivatives reversibly self-assembled to form multifunctional vesicles and applied in pancreatic cancer chemoradiotherapy. a Schematic representation of the

derivatives' reversible self-assembly into vesicles. **b** The mechanism of chemoradiotherapy in antitumor activity. **c** Synergistic tumor resistance mechanism of vesicles.

conditions, the LA-BPA derivatives undergo rapid polymerization into vesicles through ROP. This reaction is highly efficient, occurs under open-air conditions, and completes swiftly. In contrast, under slightly basic conditions, the vesicles quickly revert to monomers through a rapid depolymerization process. These LA-BPA derivatives are demonstrated pH-dependent reversible assembly into synthetic vesicles. By incorporating phenylboronic acid groups, these vesicles selectively target sialic acid on tumor cells, offering a promising approach for tumor-specific drug delivery. Our studies further reveal that these vesicles can reduce cellular levels of glutathione (GSH) and promote an increase in reactive oxygen species (ROS). This shift disrupts mitochondrial membrane potential and triggers mitophagy-induced apoptosis. In addition, we have enhanced these vesicles by introducing a BPA group, which leverages the advantageous properties of boron-based compounds. This modification has proven effective in the context of BNCT for treating pancreatic cancer. Our findings indicate that these engineered LA-BPA derivatives not only self-assemble into vesicles but also effectively combine chemotherapy with BNCT, demonstrating therapeutic efficacy in mouse models of pancreatic cancer.

Results and discussion

Preparation and characterization of LA-BPA derivatives

Eight lipoic acid-boronophenylalanine (LA-BPA) derivatives (**L^PB1-4** and **L^MB1-4**) were synthesized by coupling lipoic acid (the head) with the amino group of BPA (the tail) via a short-chain PEG linker (Supplementary Fig. 1, Note 1 and Fig. 2a–c). In this design, lipoic acid serves as the cross-linking unit, BPA at the tail functions as the targeting moiety, and the short-chain PEG acts as a hydrophilic spacer. LA-BPA derivatives without PEG spacer did not stabilize the forming vesicles (Supplementary Fig. 2). The synthesis and characterization of these LA-BPA derivatives were confirmed by nuclear magnetic resonance spectroscopy (Supplementary Note 2). The vesicles' self-assembly from LA-BPA derivatives was performed under acidic conditions, as depicted in Fig. 2d. The critical aggregation concentrations (CAC) of these compounds were determined to be below 0.3 mM (Fig. 2e and Supplementary Fig. 3a). Figure 2e and Supplementary Fig. 3b showed that the eight LA-BPA derivatives readily self-assembled into nanoparticles above their respective CACs, displaying zeta potential values of -28 to -35 mV and polymer dispersity indices below 0.3 for all samples. The dynamic light scattering data revealed that the particle size distributions broadened toward larger average sizes with increasing PEG chain length. Transmission electron microscopy (TEM) images confirmed that the nanoparticles exhibited a spherical core-shell vesicular nanostructure with high monodispersity (Fig. 2f). **L^PB-3** was synthesized with a high overall yield (Supplementary Table 1) using less expensive raw materials. The vesicles formed from **L^PB-3** featured a moderate particle size, leading to the selection of **L^PB-3** for further investigations.

Controllable assembly of L^PB-3-based vesicles and mechanisms

We then systematically analyzed the efficacy of both organic and inorganic acids in the **L^PB-3** ROP. The results, depicted in Fig. 3a, highlighted that the top four commonly used acids effectively catalyzed this ROP reaction. Interestingly, an unexpected outcome emerged when hydrochloric acid (HCl) was used as the catalyst: the pH dropped to 1.0, which was far lower than in vivo context. Simultaneously, we assessed the relationship between particle size and pH variation. As shown in Fig. 3b and Supplementary Fig. 4, the diameter of the vesicles decreased as the pH increased, whereas the zeta potential of the vesicles rose with the pH level. To alter the pH of the suspension, NaOH (2.5 M stock) was utilized for adjustments, with continuous monitoring using a pH meter. As the pH shifted from 1.0 to 8.0, the solution transitioned from a white turbid appearance to a clear solution (see in Supplementary Movie 1), indicating the depolymerization of the vesicles back into their original small-

molecular compounds as confirmed by liquid chromatography-tandem mass spectrometry and ¹H NMR (Supplementary Fig. 5). Following this observation, HCl was incrementally added to the solution. Upon reaching a pH of 7.2, the clear solution instantaneously transformed back to a white suspension, indicative of vesicle formation. This finding demonstrates that the morphological alterations of the vesicles can be repeatedly reversed through a polymerization-depolymerization cycle.

Building on these experimental findings, we aimed to create reversible compound vesicles by alternately introducing a base (2.5 M NaOH) and an acid (1 M HCl) into a water-mediated system (Fig. 3c). To achieve this, **L^PB-3** underwent three additional cycles of polymerization and depolymerization. This process was continually monitored using ultraviolet-visible spectroscopy. As showcased in Fig. 3d and Supplementary Movie 1, the distinctive absorption band at 330 nm, characteristic of **L^PB-3** monomers, emerged upon vesicle depolymerization. This observation suggests an ultrafast transition between the polymerization and depolymerization states. The vesicles experienced base-induced depolymerization without any impact on the molecular structure, and this polymerization-depolymerization cycle was found to be reversible on multiple occasions. In addition, the average size of the vesicles during this reversible formation process was determined using a nanoparticle tracking analyzer (Fig. 3e–g). These measurements revealed that repeated assembly led to the formation of smaller vesicles, characterized by a narrower and more uniform particle size distribution.

We conducted coarse-graining simulations to explore the aggregation and disaggregation processes of 35,000 **L^PB-3** molecules in water under both acidic and alkaline conditions. In an acidic environment, the **L^PB-3** molecules quickly self-aggregated into a nanoparticle within 1 μ s. Subsequently, the hydrophobic parts, colored yellow, and the hydrophilic parts, colored blue, continued to self-aggregate, resulting in a stable vesicle structure with distinct hydrophobic and hydrophilic sectors by 4 μ s (Fig. 3h, j and Supplementary Movie 2). Intriguingly, substituting the **L^PB-3** molecules in an acidic environment with those in an alkaline environment initially led the vesicle structure to transition to a disordered aggregation state, where the hydrophobic and hydrophilic areas mixed within 2 μ s. This structure then disaggregated, releasing the **L^PB-3** molecules from the disordered aggregation within 13 μ s, and eventually stabilizing into a dispersed structure with randomly distributed **L^PB-3** molecules in the solvent (Fig. 3i, k and Supplementary Movie 3). In contrast to the ROP, depolymerization of the disulfide bonds required harsher conditions and more time^{13,19}. In our experiments, we observed the recycled **L^PB-3** monomer when the pH of the water-mediated solution was increased from 7.2 to 8.0 over a prolonged period, achieving a 100% recovery rate (Supplementary Fig. 5 and Supplementary Movie 1).

Specificity of L^PB-3 vesicles for sialic acid

To reliably quantify vesicle trafficking, we employed the lipophilic fluorescent probe Cy5.5 to label the vesicles. Initially, Cy5.5@vesicles were detected through the emission of the fluorescein tag (Supplementary Fig. 6a). Confocal fluorescence imaging of these probe-labeled vesicles confirmed their characteristic annular shape and demonstrated the localization of red fluorescence to the vesicles (Supplementary Fig. 6b). Moreover, the efficiency of this labeling approach was quantified using flow cytometry, with results indicating a labeling efficiency exceeding 97% (Supplementary Fig. 6c). Collectively, these findings suggest that the lipophilic fluorophore is highly effective and specific in labeling **L^PB-3** vesicles.

Cytoplasmic uptake of Cy5.5@vesicles was observed (Fig. 4a). To further explore the vesicles' specificity for sialic acid, we assessed their uptake in PANC-1 cells, a sialic acid-expressive cell line²⁰. We also conducted a parallel experiment involving these cells and a subset treated with 0.5 U of neuraminidase to remove sialic acid residues

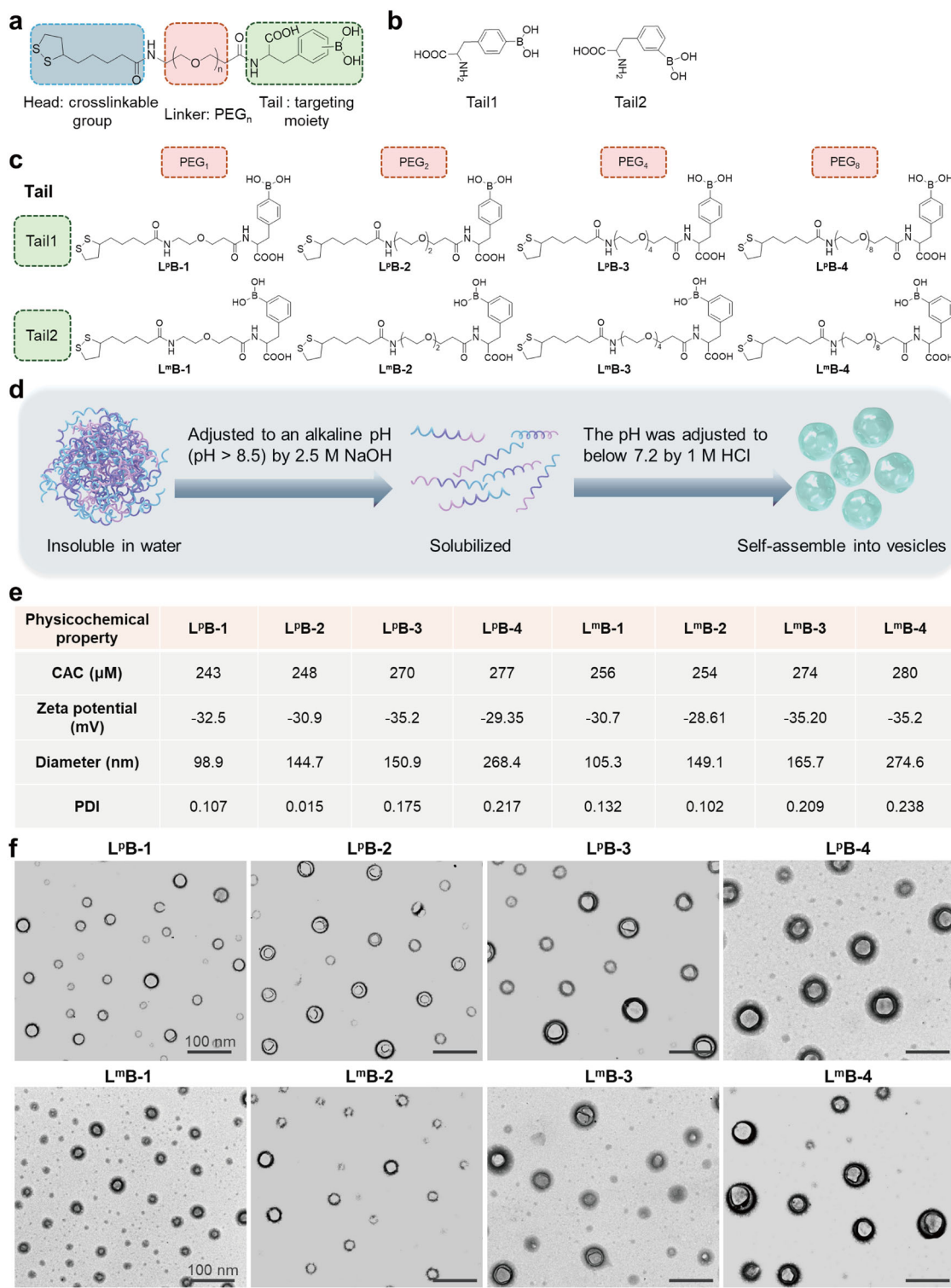
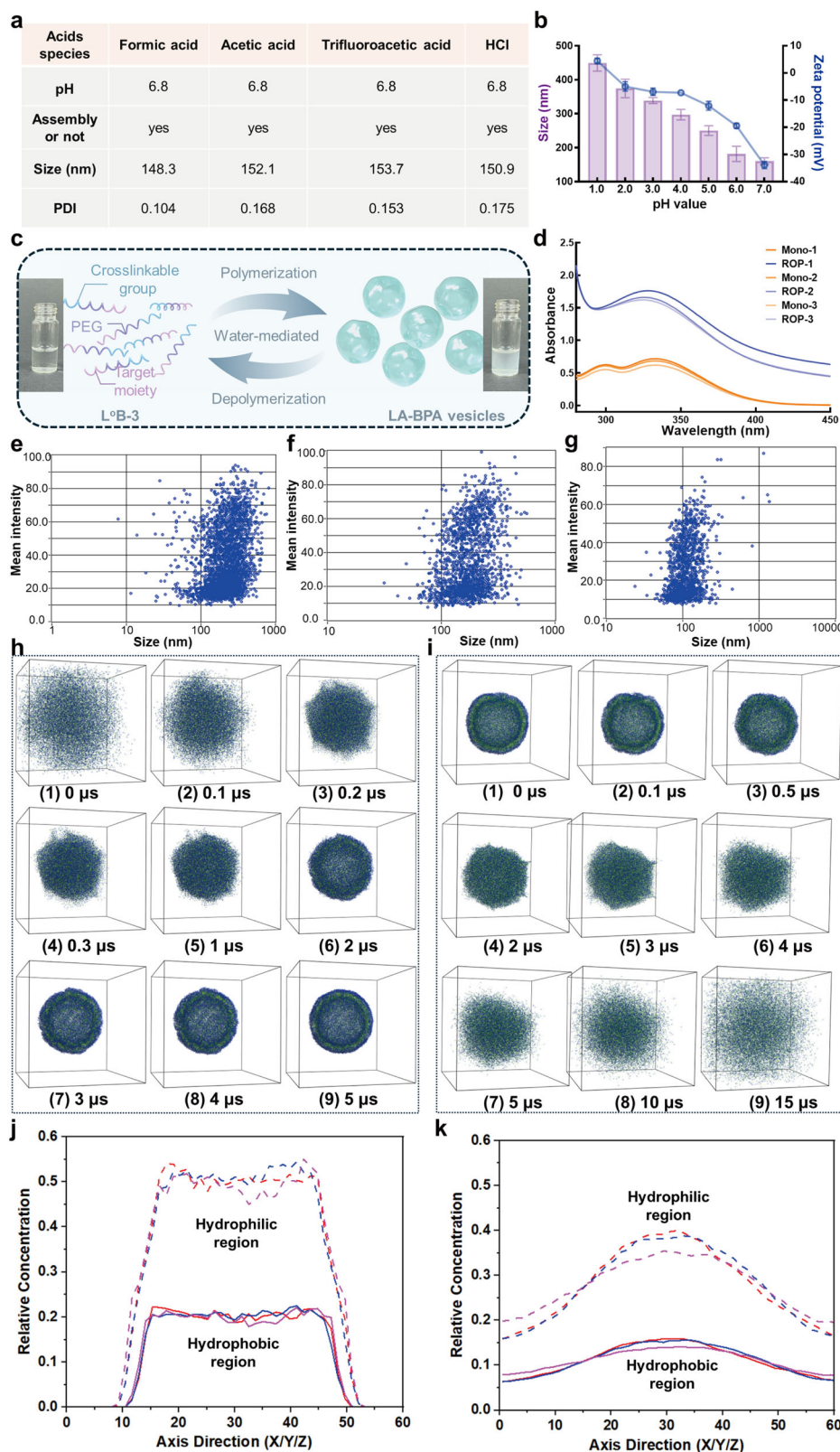


Fig. 2 | Preparation and characterization of LA-BPA vesicles. **a** Schematic view of LA-BPA derivatives, where three functional fragments are connected via amide bonds. **b** Structural formula of the targeting moiety. **c** Chemical structures of eight LA-BPA candidates. **d** Schematic representation of the vesicle production process.

e Physicochemical properties of the self-assembled vesicles. **f** Representative TEM images of the vesicles. Scale bar is 100 nm. TEM measurement of vesicles solution at 1.0 mg/mL concentration were repeated 3 times independently with similar results, and one representative image from each LA-BPA derivative was shown.

from the glycoproteins on their membrane surfaces²¹. Stronger fluorescence signals compared to those treated with neuraminidase (Fig. 4c). When Cy5.5@vesicles were pre-incubated with N-acetylneurameric acid, whose diol group would mask phenylboronic acid, the cell uptake also was reduced (Supplemental Fig. 6g). Fluorescence intensity was quantified for individual cells, the average

intensity from the normally cultured group was ~2.4 times higher than that of the neuraminidase-treated group, and about 3 times higher than that of Cy5.5@vesicles pre-treated with N-acetylneurameric acid (Fig. 4d). The unspecific uptake of nanoparticles by cancer cells is known but not as effect as with phenylboronic acid-sialic acid binding^{8,9}. The phenylboronic acid group could be fabricated for cell



adhesion, especially those cancer cells with overexpression of sialic acid⁷. The binding of the receptors targeted vesicles to tumor cells would likely lead to receptors-mediated internalization of the vesicles-sialic acid complexes, the vesicles also would be translocated to intracellular through endosomes and phagosomes pathway²². Moreover, in vitro cell uptake of the Cy5.5@vesicles against sialic acid was further investigated by MCF-10A and human primary pancreatic acinar

cells, both showed much less expression levels of sialic acid. As expected, in vitro experiments using MCF-10A and human primary pancreatic acinar cells showed that Cy5.5@vesicles uptake decreased than that of PANC-1 cells. As shown in Supplemental Fig. 6h, i, the cellular uptake study of Cy5.5@vesicles showed that more internalized Cy5.5@vesicles in cancer cells than that of in normal cells. This demonstrated that the cellular uptake level of L^PB-3 vesicles had a clear

Fig. 3 | The mechanism of L^PB-3 vesicles pH-mediated reversible self-assembly. **a** Different acids used to investigate the self-assembly of L^PB-3 vesicles. **b** Trends in particle size and zeta potential of L^PB-3 vesicles under various pH conditions. Data are displayed as mean \pm SD of $n = 3$ independent measurements. **c** Schematic representation of the acid-base mediated reversible assembly of vesicles. **d** Real-time detection of the UV-vis spectra of the aqueous solution of vesicles during the polymerization–depolymerization process. **e–g** Particle size changes in L^PB-3 vesicles during repeated depolymerization and reassembly. **h** Coarse-graining simulation of the aggregation process involving 35,000 L^PB-3 molecules in an

acidic environment; coarse-graining water molecules are not shown. **i** Coarse-graining simulation of the deaggregation process involving the same aggregation structure of 35,000 L^PB-3 molecules in an alkaline environment; coarse-graining water molecules are not shown. Relative concentration profiles of the hydrophilic part (dotted lines) and the hydrophobic part (solid lines) in the SSB molecules along the X-axis (red lines), Y-axis (blue lines) and Z-axis (magenta lines) during the last 1 μ s Coarse-Graining simulations of the model for **j** the aggregation simulation and the model for **k** the deaggregation simulation.

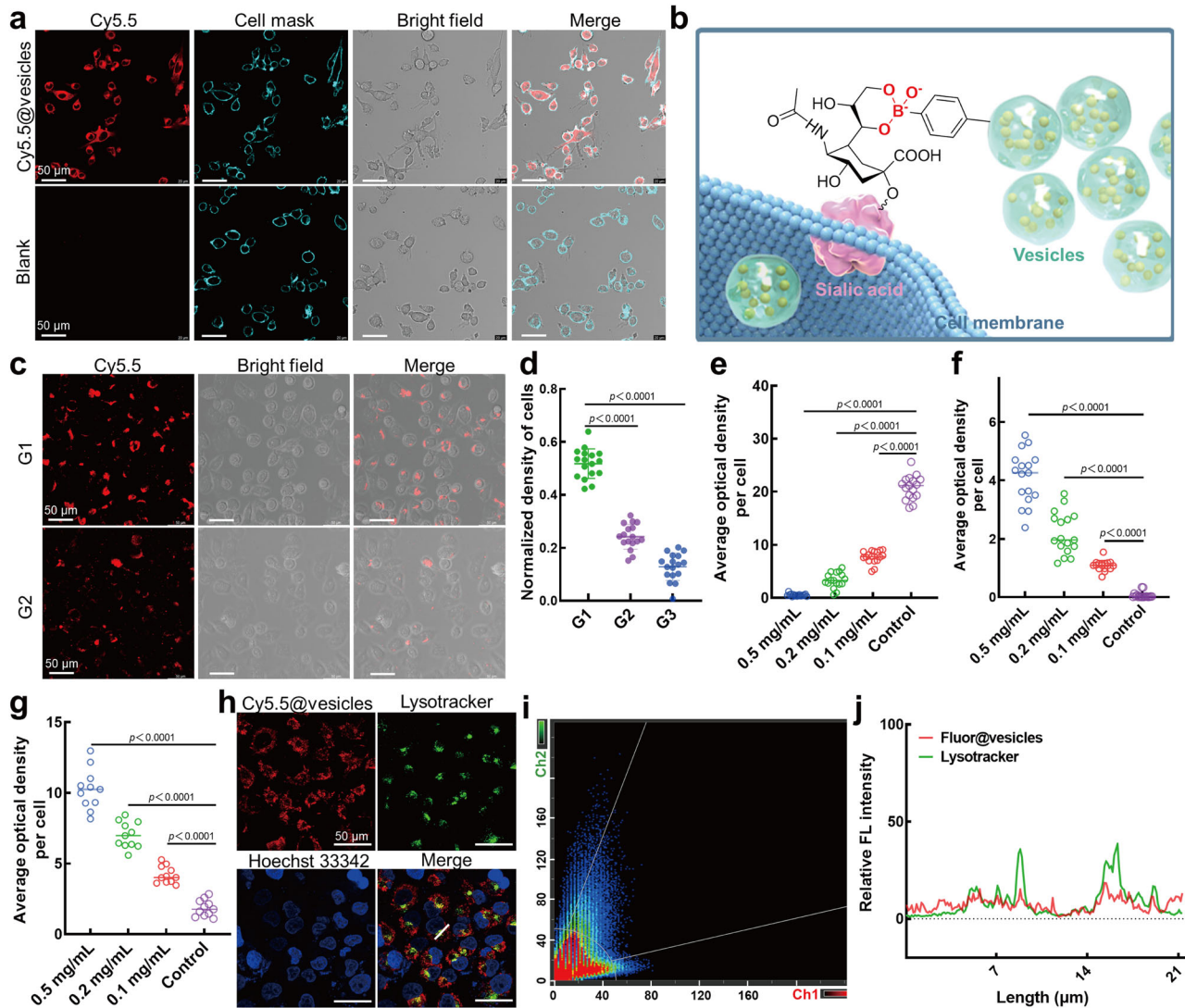


Fig. 4 | The biological effects of L^PB-3 vesicles. **a** Uptake of Cy5.5@vesicles by PANC-1 cells. **b** Sialic acid targeting mechanism of L^PB-3 vesicles. **c** Images and **d** normalized statistics of cell uptake of Cy5.5@vesicles. Cy5.5@vesicles uptake in PANC-1 cells without neuraminidase (G1) and with neuraminidase (G2, G3); cellular uptake of N-acetylneurameric acid-treated Cy5.5@vesicles ($n = 3$ independent experiments). **e** Intracellular GSH and **f** ROS levels in PANC-1 cells after 24 h incubation with various concentrations of L^PB-3 vesicles ($n = 3$ independent experiments). **g** Statistical analysis for JC-1 green fluorescence ($n = 3$ independent experiments). **h** Representative microscopic images showing co-localization of

Cy5.5@vesicles (red) and Lysotracker (green) in PANC-1 cells. **i, j** Analysis of the co-localization between Cy5.5@vesicles and Lysotracker performed using Leica Colocalization Viewer Software. A Pearson coefficient value greater than 0.5 indicates co-localization between the two signals. Scale bar is 50 μ m in (a, c, h). Data are displayed as mean \pm SD of $n > 10$ independent measurements in (d–g). Each experiment was repeated 3 times independently with similar results in (a, c, h). P values in (d–g) were determined by One-way ANOVA analysis followed by Tukey's multiple comparisons test. *** $p < 0.0001$.

dependence on targeting sialic acid, and the phenylboronic acid on the vesicles' surfaces facilitated targeted delivery to sialic acid-expressive cells (Fig. 4b). Based on these results we continued to address the degradation of intracellular L^PB-3 vesicles. When the PANC-1 cells were treated with Cy5.5@vesicles for over 36 h, the majority of

fluorescence signal redistributed from cytosol to the mitochondrial, a subcellular co-localization assay showed that Pearson coefficient was 0.793, which demonstrated the high correlation of intensity distribution between the two channels (Supplemental Fig. 6l). This change might be explained by the free Cy5.5 released from vesicles. After that

positively charged Cy5.5 probe was further adsorbed to the negatively charged mitochondrial membrane.

Adjuvant properties of L^PB-3 vesicles for antitumor in vitro

Disulfide-assisted nanomaterials and probes have emerged as effective strategies for drug delivery, not only in anticancer therapy but also for depleting glutathione (GSH)^{21,23,24}. The intracellular GSH levels in cells exposed to varying concentrations of vesicles for 24 h. The GSH assay results showed that intracellular GSH levels decreased as the vesicle concentration increased (Supplementary Fig. 7a). Specifically, the average fluorescence indicating GSH levels was ~33 times lower at a vesicle concentration of 0.5 mg/mL compared to the control group (Fig. 4e), which was consistent with our hypotheses. Considering GSH's role as a primary cellular antioxidant, its substantial reduction can enhance reactive oxygen species (ROS) levels, leading to decreased mitochondrial membrane potential and compromised mitochondrial integrity. We measured intracellular ROS levels using HDCF-DA and observed that the ROS levels were inversely related to GSH levels. Higher ROS levels corresponded with diminished GSH levels and increased with the vesicle concentration (Fig. 4f and Supplementary Fig. 7b). This inverse correlation was confirmed by further tests, indicating that GSH depletion within cells led to an accumulation of ROS. Considering the high sensitivity of intracellular mitochondria to ROS, we induced JC-1 to evaluate the cellular mitochondria status. Aggregates of JC-1 indicate healthy polarized mitochondria (red), whereas monomers of JC-1 indicate unhealthy depolarized mitochondria (green). The mitochondrial membrane potential was assessed using MitoProbe JC-1 and imaged with confocal laser microscopy (Fig. 4g and Supplementary Fig. 7c). Untreated PANC-1 cells displayed abundant JC-1 aggregates, indicative of healthy mitochondria, whereas treatment with vesicles resulted in predominantly JC-1 monomers, suggesting a loss of mitochondrial potential. Overall, the disulfide bond cleavage in L^PB-3 vesicles effectively depleted GSH, disturbing the balance between intracellular GSH and ROS and leading to increased ROS production. This elevated ROS level within the cancer cells consequently induced mitochondrial damage, thereby inhibiting cell proliferation.

The phenylboronic acid-mediated lysosome escape of L^PB-3 vesicles

Lysosomal entrapment impedes the effective subcellular delivery of anti-tumor therapeutic agents. Timely lysosomal escape is crucial for nanomedicine to avoid premature degradation in the acidic lysosomal environment. Previous studies have demonstrated that incorporating phenylboronic acid into nanomaterials enhances cellular uptake and facilitates lysosomal escape^{9,25}. In our study, we examined the lysosomal escape behaviors of Cy5.5@vesicles, using colocalization with LysoTracker Green (Fig. 4h). For this analysis, we used the red fluorescence of Cy5.5@vesicles and the green fluorescence of lysosomes, with results presented in Fig. 4i,j. Pearson's coefficient was calculated to assess colocalization; however, the fluorescence overlap between the two channels was minimal, resulting in a low Pearson's colocalization coefficient of 0.305. Notably, colocalization is defined as having a coefficient of 0.5 or higher²⁶. To test this, we investigated the Cy5.5@vesicles distribution using chloroquine (40 μM, 1 h) to inhibit lysosomal function before adding Cy5.5@vesicles. As shown in Supplementary Fig. 6j, there were no change in the amount and distribution of Cy5.5@vesicles. For colocalization, the Pearson coefficient was 0.341, which denoted no co-localization. But when phenylboronic acid was blocked with N-acetylneurameric acid, the colocalization coefficient with the lysosome increased up to 0.857 (Supplementary Fig. 6k). This observation suggested that blocking phenylboronic acid would enhance Cy5.5@vesicles' interaction with lysosome. These findings validate our hypothesis that L^PB-3 vesicles provide a platform to aid lysosomal escape, thereby circumventing

premature degradation in the acidic conditions of lysosomes. These findings validate our hypothesis that L^PB-3 vesicles provide a platform to aid lysosomal escape, thereby circumventing premature degradation in the acidic conditions of lysosomes. This attribute positions L^PB-3 vesicles as an ideal nanocarrier for drug delivery in tumor-targeted therapy, by reducing lysosomal degradation.

Drug loading and release in the L^PB-3 vesicles

Similar to liposomes, L^PB-3 vesicles show promise in drug delivery, characterized by their aqueous core which is capable of encapsulating hydrophilic agents. Doxorubicin hydrochloride (Dox), illustrated in Supplementary Fig. 8a, was used as a model drug in our nanomedicine preparation. To establish a correlation between the peak area of HPLC and Dox concentration, we plotted a calibration curve, as shown in Supplementary Fig. 8b. This curve demonstrated a strong linear relationship, with an R² value of 0.99. Using this standard curve, outlined in Supplementary Fig. 8c, we calculated the total Dox content and the entrapment efficiency within L^PB-3 vesicles. The experimental data revealed that the encapsulation efficiency diminished as the Dox amount increased, likely due to the vesicles' finite drug loading capacity. Optimal encapsulation was observed at a drug-to-vesicle mass ratio of 1:10, achieving an 81% encapsulation efficiency and a drug loading of 7.8%. The average particle size and zeta potential of Dox@vesicles were measured at 160.5 nm and -27.85 mV, respectively (Supplementary Fig. 8d, e). There was no notable difference in particle size between the drug-loaded and unloaded vesicles, suggesting that the drug, confined within their cores, minimally influenced the hydrodynamic size. We assessed the in vitro stability of Dox@vesicles by dispersion in PBS for 24 h, and as anticipated, there was no alteration in particle size during this period, as reported in Supplementary Fig. 8f. Morphological evaluations of Dox@vesicles under various conditions were documented in Supplementary Fig. 8g. The vesicles retained their morphology in both water and culture medium; however, exposure to 5 mM or 10 mM GSH led to disorganized surfaces and visible edge breakage, facilitating on-demand Dox release (Supplemental Fig. 8h).

We also investigated the in vitro release of Dox from L^PB-3 vesicles induced by GSH in various simulated environments, including PBS (pH = 7.2) with or without GSH (5 mM). As shown in Supplementary Fig. 8h, Dox@vesicles exhibited limited release of Dox in PBS, with only 32.2% released over 48 h, indicating minimal drug leakage under physiological conditions. However, the presence of 5 mM GSH accelerated drug release, with a cumulative release of 93.8% over the same period, demonstrating the vesicles' responsiveness to GSH. Given that GSH, a hydrophilic molecule, is prevalent in tumor cells, it serves as an intracellular trigger for drug release specifically at tumor sites. This is beneficial for minimizing potential side effects and enhancing therapeutic efficacy, as it restricts Dox release primarily to tumor cells, limiting exposure in the circulatory system.

Pancreatic cancer, a highly lethal cancer, is regarded as the second highest cause of cancer-related deaths by 2030²⁷, and breast cancer is the malignant tumor with the highest incidence among women in the world²⁸. We subsequently assessed the cytotoxic effects of Dox@vesicles compared to free Dox in the normal cells (human primary pancreatic acinar cells and MCF-10A cells) and cancer cells (human pancreatic cancer cell line PANC-1 and the human breast cancer cell line MDA-MB-231) (Supplementary Fig. 8i,j). The IC₅₀ for free Dox was determined to be 32.24 nM, while the Dox@vesicles exhibited a slightly higher IC₅₀ of 43.19 nM in PANC-1 cells, whereas in human primary pancreatic acinar cells, the IC₅₀ values of free Dox and Dox@vesicles were 31.00 nM and 149.30 nM. Similarly, the IC₅₀ values for Dox and Dox@vesicles against MDA-MB-231 cells were 55.03 nM and 38.83 nM. In MCF-10A cells, IC₅₀ values were 33.40 nM and 120.60 nM, respectively. These results indicated that the Dox@vesicles exhibited much more cytotoxicity in cancer cells than that of in normal

cells, which might be attributed to the sialic acid targeting of vesicles. The IC₅₀ values of Dox against cancer cells were lower than that of Dox@vesicles. This diminished cytotoxicity of the Dox@vesicles can be ascribed to their sustained release properties. Moreover, the cellular GSH content in cancer cells is much higher than that in normal cells, which is furthermore favorable to specifically releasing the Dox in cancer cells rather than in normal cells to avoid side effects.

Dox@vesicles for antitumor chemotherapy

L¹⁰B-3 vesicles have demonstrated notable potential in cellular uptake, lysosome escape, drug loading, and on-demand release. By employing a design strategy that leverages phenylboronic acid-sialic acid interactions in tumor tissues, these vesicles exhibit minimized non-specific interactions with normal tissues, thus enhancing tumor selectivity. To further investigate the properties of **L¹⁰B-3** vesicles as tumor suppressors *in vivo*, we monitored the antitumor efficacy of Dox@vesicles and free Dox. Both were administered at a dose of 4 mg/kg (Dox equivalent) to subcutaneous MDA-MB-231 and PANC-1 tumor-bearing mice, as delineated in our experimental flow chart (Fig. 5a) and the experimental groups (Fig. 5b). The volumes of tumors in both models were recorded over time (Fig. 5c, d, h, i). During the study, the control and saline groups' tumor volumes increased most rapidly, exceeding 1500 mm³. In contrast, the vesicles exhibited tumor-suppressing activity, especially at the initial stages of the experiment, although this rate of suppression decreased as the experiment progressed. Both Dox formulations showed antitumor efficacy, with Dox@vesicles outperforming free Dox. Tumor weights for each group are presented in Fig. 5e, j, correlating with the tumor volume data. Body weight changes over time for all experimental groups are shown in Fig. 5f, k. Both the Dox@vesicles formulation and the blank vesicles demonstrated minimal toxicity (Supplementary Fig. 9), suggesting good biocompatibility of **L¹⁰B-3** vesicles and a well-tolerated dose level of Dox@vesicles. Notably, the body weight of the free Dox group decreased compared to other groups, indicating that **L¹⁰B-3** vesicles might reduce the side effects of free drugs. The overall survival rate of all groups in the MDA-MB-231 model was assessed and illustrated in Fig. 5g. The control and saline groups succumbed within 32 days, while therapies with free Dox led to a survival advantage, totaling 60 days. The Dox@vesicles groups exhibited a median survival exceeding 60 days. These findings are supported by immunofluorescence staining of Ki67 and TUNEL on tumor tissue sections (Supplementary Fig. 10a). Ki67 staining indicated high tumor cell proliferation in the control, saline, and vesicle groups, with no signs of apoptosis. Conversely, both Dox treatment groups showed reduced Ki67 staining, indicating reduced proliferation. TUNEL staining revealed widespread apoptosis in tumor tissues from these treatment groups. Histological analysis of major organs (heart, liver, spleen, lung, and kidney) was conducted to assess potential organ toxicity (Supplementary Fig. 10b). In addition, the overall survival of PANC-1 bearing mice was under 25 days. All Dox treatments improved survival compared to the control group, but efficacy was higher in the Dox@vesicles than in free Dox (Fig. 5l). The immunofluorescence staining of Ki67 and TUNEL on frozen mouse tumor tissue sections further confirmed these results (Supplementary Fig. 11a). There were no abnormalities in the heart, spleen, lung, and kidney (Supplementary Fig. 11b), except in the liver (Fig. 5m). Hematoxylin and eosin (H&E) staining revealed notable tumor metastases in the liver from the control, saline, and vesicle groups, but not in the Dox and Dox@vesicles treatment groups. The staining of Ki67 in these lesions indicated high cellular proliferation.

Application of vesicles in pancreatic cancer boron neutron capture therapy

Encouraged by the medicinal role of boron-containing compounds, especially as agents for BNCT^{29–31}, we synthesized the **L¹⁰B-3** derivative, which contains the boron isotope B-10, using this approach

(Supplementary Fig. 12). We conducted isotopomer analysis of **L¹⁰B-3** using a high-resolution mass spectrometer (Supplementary Fig. 13a) and ¹H NMR (Supplementary Fig. 13b). Given the high mortality rates due to metastasis in pancreatic cancer models, we assessed the *in vitro* BNCT efficacy against PANC-1 cells (Supplementary Fig. 14) and *in vivo* BNCT efficacy of **L¹⁰B-3** vesicles using a xenograft pancreatic cancer model.

Before assessing *in vivo* efficacy, insights into nano-bio interactions in PANC-1-bearing mice were obtained by tracing the behaviors of Cy5.5@vesicles and free fluorophores through near-infrared fluorescence imaging. As depicted in Fig. 6a, the fluorescence signal from Cy5.5@vesicles was detectable in the tumors, livers, and kidneys from 1 to 6 h post-injection (p.i.), with the strongest signal observed at 6 h p.i. In comparison, the free fluorescent probe group displayed prominent signals in the abdomen rather than at the tumor sites, demonstrating the superior tumor-targeting efficacy of **L¹⁰B-3** vesicles. In line with the *in vivo* imaging results, the *ex vivo* imaging of the excised tissues from Cy5.5@vesicles at 6 h p.i. (Fig. 6b, c) indicated that the tumor exhibited the most intense fluorescent signal relative to other organs. This observation suggests that 6 h p.i. could represent the optimal timing for neutron irradiation of the **L¹⁰B-3** vesicles. To study the invasion of Cy5.5@vesicles in tumor site, living confocal imaging was used to investigate the intracellular distribution of Cy5.5@vesicles at 6 h post injection. As shown in Supplementary Fig. 15, although the tumor vessels were labeled with dextran-FITC and cell nuclei were tagged with Hoechst 33342 in the two groups, no obvious fluorescent signal was observed in the vicinity of cell nuclei in the group of free Cy5.5; but the fluorescent signal emitted by Cy5.5 was predominantly on the side of the cell nuclei. As shown, red fluorescent signal was observed in tumor cells of Cy5.5@vesicles, while that of the free Cy5.5 group showed no signal. This result also indicated that the vesicles were enough stable in circulation, which made it conducive to delivering drug over a long period. These results supported that the **L¹⁰B-3** vesicles were stable enough to delivery small molecular compounds to tumor site and a promising tumor-target nanocarrier.

Before neutron irradiation, we assessed the distribution of B-10 across major organs in two dosage groups: low (250 mg/kg) and high (350 mg/kg). The distribution patterns of B-10, as depicted in Fig. 6d, e, aligned with those observed in *ex vivo* imaging. In each group, tumor tissues exhibited the highest content of B-10, with notably higher accumulation observed in the high-dose group. Specifically, B-10 concentrations were measured at 23.35 ppm in the high-dose group and 15.48 ppm in the low-dose group. In the group receiving the higher dose, the B-10 concentration in the tumor was 5.0 times that of the blood, compared to 4.6 times in the low-dose group, as indicated in Fig. 6f. Furthermore, the tumor-to-normal tissue ratio was 7.7 in the high-dose group and 6.9 in the low-dose group. These findings suggest that **L¹⁰B-3** vesicles can prolong circulation time *in vivo* and enhance the accumulation of B-10 at the tumor site, ultimately improving the tumor-to-blood and tumor-to-normal tissue ratios compared to free BPA.

To further assess the antitumor efficacy of **L¹⁰B-3** vesicles in BNCT, we conducted an *in vivo* study using PANC-1 tumor-bearing mice. The evaluation workflow is depicted in Fig. 6g. Female mice bearing PANC-1 tumors received injections of saline (200 µL), high-dose **L¹⁰B-3** vesicles (350 mg/kg, BNCT H), or low-dose **L¹⁰B-3** vesicles (250 mg/kg, BNCT L), 6 h before neutron irradiation. Both the BNCT H and BNCT L were injected vesicles through the tail vein, respectively, 6 h latter received neutron irradiation. The control and neutron irradiation groups were injected with an identical volume of saline, the neutron irradiation group received neutron irradiation, whereas the control group received no irradiation. Dosimetric assessment of photon and proton exposure was performed using Monte Carlo simulations. As shown in Fig. 6h, the resulting radiation doses to the tumor tissues were 1.50 Gy for BNCT H group, 1.19 Gy for

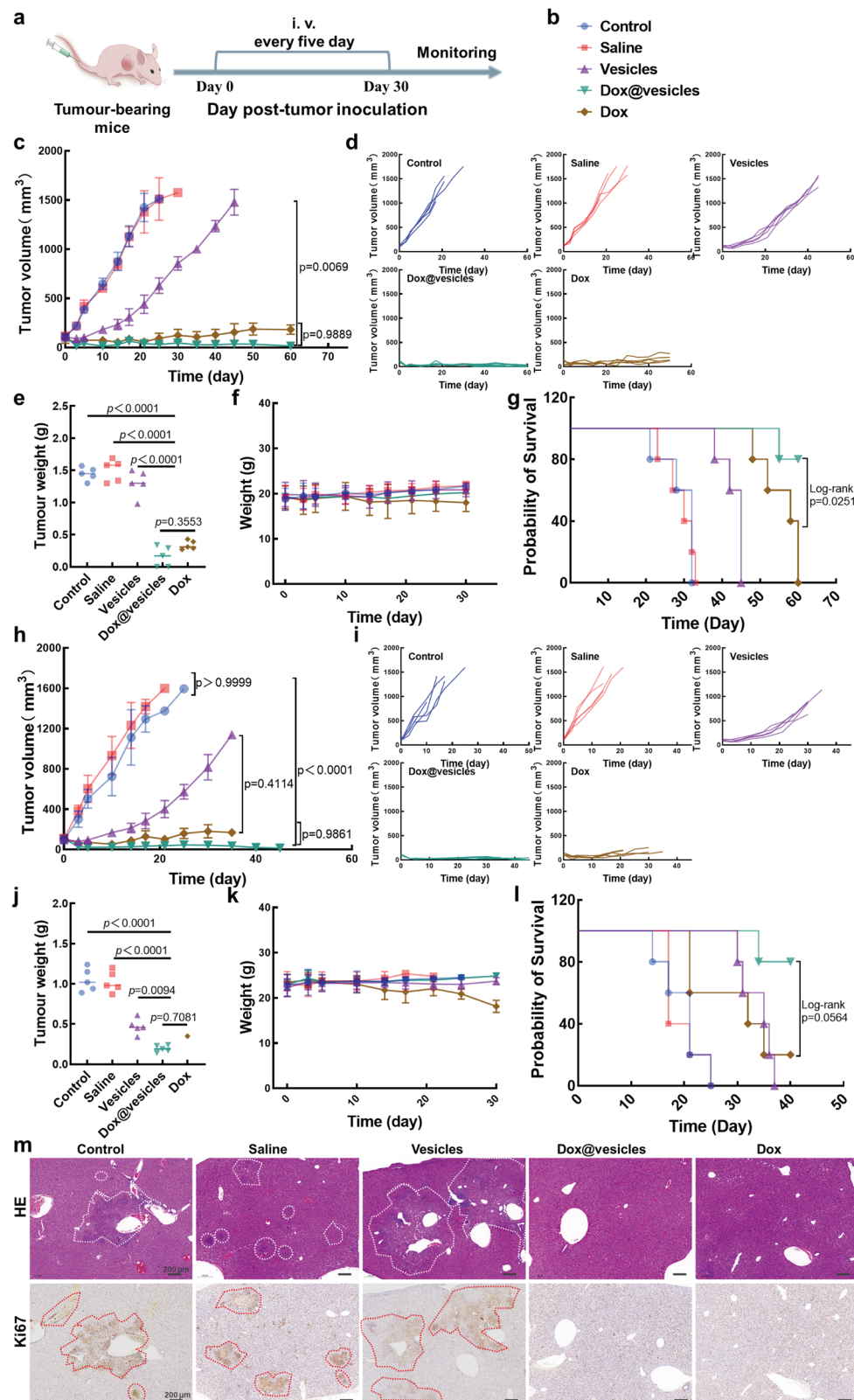
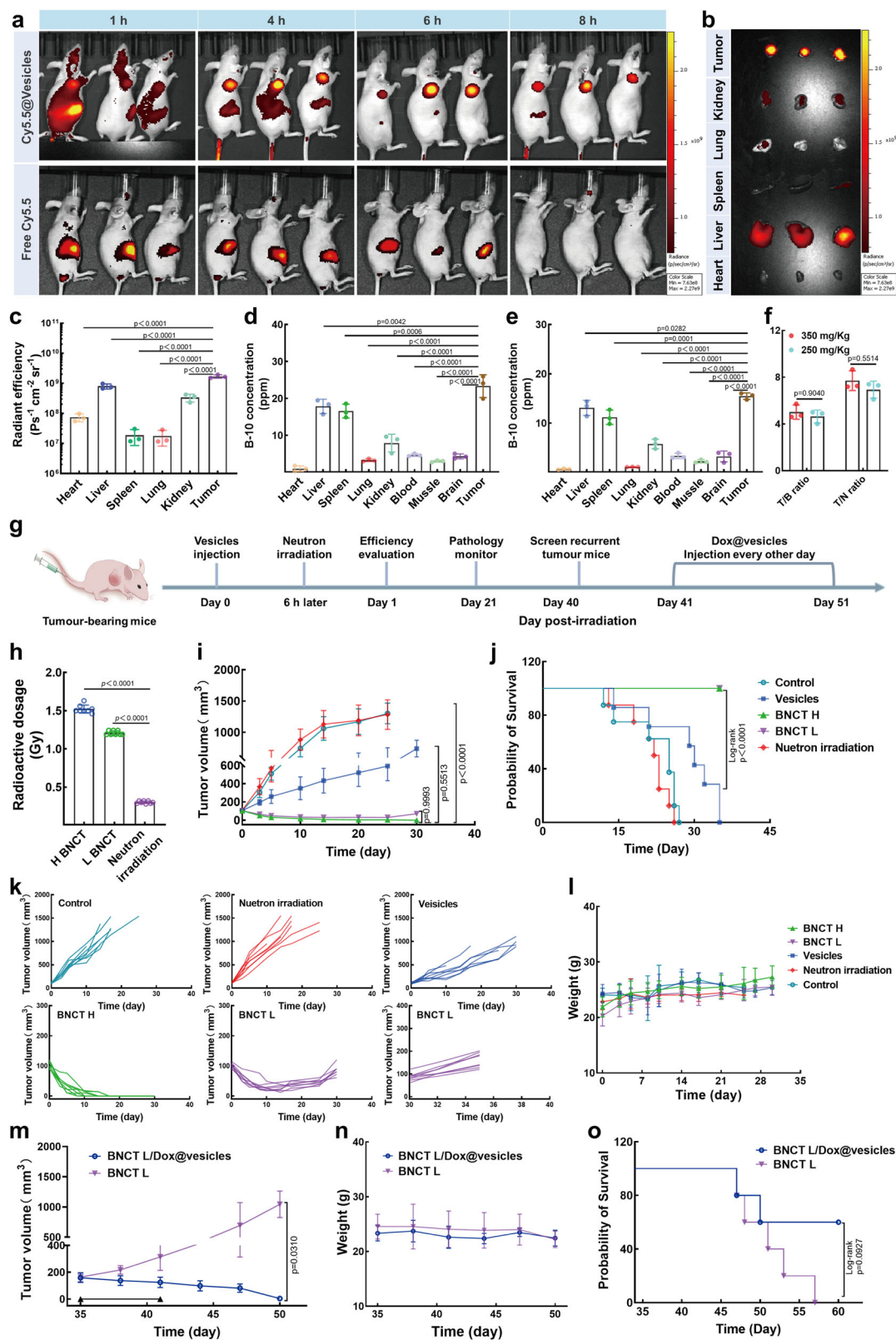


Fig. 5 | Dox@vesicles for enhanced antitumor effect. **a** Schematic illustration of the experimental flow. **b** Animals were randomized before treatment ($n=5$ mice per group). **c** Tumor volume of MDA-MB-231 bearing mice growth curves. **d** Tumor growth curves for individual MDA-MB-231 model mice. Mice were monitored for **e** tumor weight and **f** body weight. **g** Kaplan-Meier curves for overall survival. **h** Tumor growth curves of PANC-1 bearing mice treated with different regimens. **i** Individual tumor growth curves. **j** Tumor weights and **k** body weights of mice over

time. **l** Kaplan-Meier curves for overall survival. **m** The HE and Ki67 staining of liver tissues. Each experiment was repeated 3 times independently with similar results in **m**. Scale bar is $200\text{ }\mu\text{m}$. Data are displayed as mean \pm SD of $n=5$ independent measurements in **(c, e, f, h, j, k)**. *P* values in **(e)** and **(j)** were determined by One-way ANOVA analysis followed by Tukey's multiple comparisons test. n.s., not significant (ANOVA), ** $p < 0.01$, *** $p < 0.0001$.



BNCT L group, and 0.20 Gy for the group subjected only to neutron irradiation.

Tumor volume and mouse survival were monitored following therapy. Mice injected with saline and subjected to neutron irradiation exhibited the fastest tumor growth (Fig. 6i, k), indicating that neutron irradiation alone did not suppress tumor development. In contrast, tumors treated with vesicles demonstrated slower growth. In the

BNCT L group, treated with low-dose vesicles and subjected to neutron irradiation, tumor volume initially decreased but later recurred, indicating partial efficacy but insufficient for treating mice bearing PANC-1 tumors. Conversely, in the BNCT H group, tumor growth was completely inhibited 15 days after neutron irradiation, with no signs of tumor recurrence by day 30. This indicates that **L**¹⁰**B**-3 vesicles in BNCT effectively eradicated PANC-1 growth at a dose of 350 mg/kg. Further,

Fig. 6 | L¹⁰B-3 vesicles as targeted B-10 agents for BNCT combined Dox@vesicles in PANC-1 models radiochemotherapy. **a** The biodistribution of Cy5.5@vesicles was monitored using the IVIS imaging system. **b** Following the intravenous injection of Cy5.5@vesicles, the biodistribution was assessed in major organs at 6 h. **c** Corresponding fluorescence intensities in major organs at 6 h post-intravenous injection. **d** B-10 content in the major organs for the group receiving vesicle doses of 350 mg/kg. **e** B-10 content in the major organs for the group receiving vesicle doses of 250 mg/kg. **f** The tumor/normal tissue ratio and tumor/blood ratio of B-10 content in the two dosage groups. **g** Schematic illustration of the experimental flow. **h** Quantification of incorporated radioactivity. **i** Subcutaneous

tumor volume growth curves. **j** Overall survival estimated by Kaplan–Meier curves. **k** Tumor growth curves for individual mice. **l** Body weight curves of PANC-1 bearing mice in each experimental group. **m** Tumor growth curves after Dox@vesicles injection indicating recurrence. **n** Statistical analysis of body weight and **o** overall survival between BNCT alone and BNCT combined with Dox@vesicles over 15 days post-Dox@vesicles injection. Data are displayed as mean \pm SD of $n = 3$ independent measurements in (c–f), $n = 8$ independent measurements in (h–l), and $n = 5$ independent measurements in (m–o). P values in (h) were determined by One-way ANOVA analysis followed by Tukey's multiple comparisons test. n.s., not significant, * $P < 0.05$, ** $p < 0.01$, *** $p < 0.001$, **** $p < 0.0001$.

the survival rate was 100% in both BNCT groups on day 35, higher than in other groups (Fig. 6j), underscoring the therapeutic efficacy of our designed vesicles as boron-containing agents in BNCT. Body weight measurements during treatment, shown in Fig. 6i, revealed a gradual increase in all mice, suggesting that the treatment was free from systemic toxic effects. Overall, these results suggest that using L¹⁰B-3 vesicles in BNCT could be a promising strategy to enhance therapeutic efficacy against pancreatic cancer by inhibiting tumor growth.

Dox@vesicles as a supplement for tumor recurrence of BNCT L
In clinical practice, single-treatment approaches often fall short in achieving satisfactory therapeutic outcomes, thus making combination treatments a preferred method for enhancing therapeutic benefits. Considering the L¹⁰B-3 vesicles for targeted Dox delivery, we further explored the therapeutic efficacy of Dox@vesicles in treating tumor recurrences in BNCT L. Animals in the BNCT L group were randomly divided into two groups: one treated with Dox@vesicles and the other left untreated. Measurements of tumor volume, as shown in Fig. 6m, indicated that the untreated mice exhibited rapid tumor growth, with an increase of approximately 7.5-fold over 15 days. In contrast, this increase was reduced by half in the BNCT L group treated with Dox@vesicles. Throughout the treatment period, there was no reduction in body weight among the animals, as depicted in Fig. 6n. In addition, the median survival time for the BNCT L/Dox@vesicles group was 60 days, compared to overall survival of 57 days for the untreated group (Fig. 6o). These results demonstrate that Dox@vesicles, either as a standalone treatment or in conjunction with BNCT.

At the conclusion of the experiment, a pathological analysis was performed. H&E staining showed no necrosis and edema in most organs, except for the kidney and spleen accompanied by relatively mild inflammatory in BNCT H and BNCT L groups (Supplementary Fig. 16a). Notably, multiple tumor lesions were identified throughout the livers of the control, neutron irradiation, and vesicles groups (Supplementary Fig. 16b). In addition, sections of the liver were stained for Ki67, a marker indicative of tumor cell proliferation. These sections showed high proliferative activity within the lesions. Immunofluorescence staining indicated that Ki67 expression was reduced in the BNCT L group and was lowest in the BNCT L/Dox@vesicles and BNCT H groups, in comparison to the control group. The expression levels in the neutron and vesicles groups were comparable to that of the control (Supplementary Fig. 17). This observation was supported by TUNEL staining, which demonstrated a more extensive area of apoptosis in the BNCT H and BNCT L/Dox@vesicles groups than in the control group, with the BNCT L group also showing apoptosis. Similar to the control, the neutron irradiation and vesicles groups exhibited almost no signs of apoptosis. These findings suggest that supplementing radiotherapy with Dox@vesicles could potentially enhance the efficacy of standalone BNCT in inhibiting tumor growth and extending survival.

Undoubtedly, this exploratory study inevitably has certain shortcomings. One drawback of L¹⁰B-3 vesicles is the potential mechanism instability of these nanocarriers, which result in the storage difficulties. Another obvious disadvantage of L¹⁰B-3 vesicles is that the

phenylboronic acid inevitably leads to non-specific interactions with endogenous polyhydroxy compounds such as glucose, which possess a degree of risk when the vesicles regarded as drug delivery carriers. Thus, the delivery method for chemotherapeutic agent must be taken into account and optimized, and this could be a challenging process. When applied to BNCT, the B-10 content is reduced compared to the active pharmaceutical ingredient BPA.

L¹⁰B-3 vesicles as BNCT agents for melanoma treatment

Melanoma is one of the deadliest forms of skin cancers and lacks effective treatments. It is well-known that BNCT provides a binary therapeutic technique by eliminating tumor cells and sparing normal cells for melanoma. To better understand the role of L¹⁰B-3 vesicles in BNCT, we further explored the vesicles applied in BNCT for melanoma treatment. For monitoring the vesicles distribution in vivo, fluorescence imaging was performed by IVIS spectrum (Fig. 7a), which showed vesicles were enriched at tumor sites to reach the maximum amount at 6 h post injection, and then decreased. A biopsy was performed to allow for ex vivo IVIS imaging of the tumor tissues and major organs at 6 h post injections. As shown in Fig. 7b, fluorescence distribution also appeared in liver, kidney, and spleen, but the strongest signal was detected in tumor site. L¹⁰B-3 vesicles was given in a single dose at a dose rate of 350 mg/kg. Then, we tested the B-10 concentrations of different organs by ICP-MS at the same time point. The highest B-10 content in tumor sites was observed, followed by liver and kidney (Fig. 7c, d). By contrast, L¹⁰B-3 vesicles generated more B-10 distribution on tumor sites than in normal tissues and blood, with T/N ratio of 6.7 and T/B ratio of 4.1, respectively. As shown in Fig. 7e, f, a rapid tumor volume growth of B16F10 tumor was observed in control, vesicles, and neutron irradiation groups, which was decreased in BNCT group. Meanwhile, the animals of all experimental groups showed a slow increase in body weight (Fig. 7g), indicating no systemic side effects during the experiment period. The curves results showed that BNCT group had the longest survival time than the other groups (Fig. 7h). The overall survivals were 18, 19, 20, and more than 35 for the control, neutron irradiation, vesicles and BNCT group, respectively. The overall survival of the BNCT group compared with controls was increased. The HE staining results showed no obvious abnormal lesions in the major organs of the other groups compared with control group (Supplementary Fig. 18). The HE staining of tissue sections indicated the nuclei presented in cancer cells after BNCT treated became fragmentized and disappeared, suggested cell apoptosis and necrosis (Fig. 7i). In contrast, nuclei of the other groups' cells were intact and appeared normal morphology as visualized by HE staining. This result was further evidenced by the Ki67 and TUNEL staining (Fig. 7j), the TUNEL staining revealed notably apoptotic signal in tumor tissues and fewer proliferating tumor cells after BNCT treatment compared to other groups. Taken together, these results showed that L¹⁰B-3 vesicles as a promising boron nanomedicine was a promising option for the BNCT of melanoma.

In summary, we synthesized LA-BPA derivatives and developed a simple method for creating multifunctional vesicles in an acidic environment. These vesicles dissociate completely into monomers

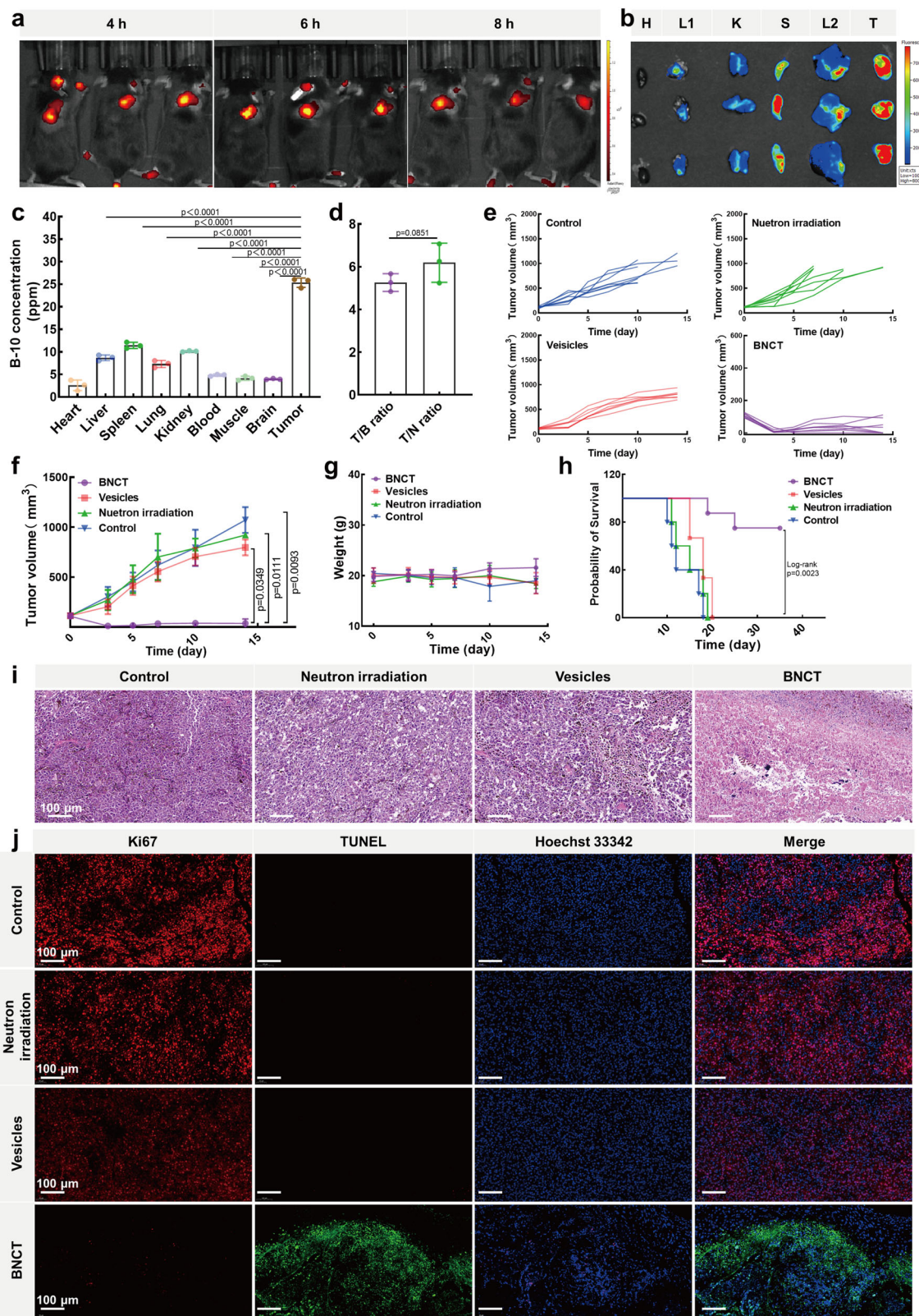


Fig. 7 | Antitumor effect in B16F10 tumor model. **a** Representative images of Cy5.5@vesicles recruitment in B16F10 tumor-bearing mice. **b** Ex vivo live imaging of dissected organs and tumor tissues from mice as performed 6 h after intravenous of Cy5.5@vesicles, H: heart, L1: lung, K: kidney, S: spleen, L2: liver, T: tumor. **c** Quantification of B-10 content in major organs and tumor tissue. **d** The B-10 ratios of target/nontarget organs at 6 h post intravenous. **e** Growth curves of individual

tumor. **f** Mean tumor growth curves of mice in each group. **g** The body weight of animals in each group. **h** Survival curves of the mice in different groups. **i** HE staining and **j** Ki67 immunohistochemical staining and apoptosis testing of tumor tissue sections from experimental groups. Data are displayed as mean \pm SD of $n = 3$ independent measurements in (c) and (d), $n = 7$ independent measurements in (f) and (g). n.s., not significant, * $P < 0.05$, ** $P < 0.01$, *** $P < 0.0001$.

under basic conditions. A primary potential application for these vesicles is their hollow aqueous core, which can carry and distribute Dox by encapsulation, achieving a drug loading capacity of 7.8% with a drug-to-vesicles mass ratio of 1:10. Importantly, the presence of phenylboronic acid on the vesicle surface facilitates lysosome escape and targets sialic acid, enhancing tumor targeting while reducing off-target selectivity, thereby improving anti-tumor efficacy. In addition, we synthesized a B-10 isotope derivative using the same strategy, and used it to prepare vesicles containing 1.6% B-10 element. These B-10 enriched vesicles showed strong anti-tumor effects when used in conjunction with neutron irradiation. The anti-tumor efficacy of **L¹⁰B-3** vesicles as BNCT nanomedicine was validated by using PANC-1 and B16F10 bearing animal. Moreover, administering Dox@vesicles following this treatment helped eradicate recurrent PANC-1 tumors. Therefore, we believe that these LA-BPA derivatives represent innovative monomers for vesicle fabrication, promising as sialic acid-targeting nanoplatforms for chemoradiotherapy with potential for clinical application.

Methods

Ethical statement

All animal experiments were performed following the protocols approved by the Ethics Committee of the Animal Experimental Center of State Key Laboratory of Biotherapy of Sichuan University (Checking number: 20210409028). The ethics committees allowed a maximum tumor size of 20 mm, and this study did not exceed during the course of the experiment.

Reagents and apparatus

All reagents and chemicals were purchased from Sigma-Aldrich, J&K Scientific, Energy Chemical, and Bide Pharm. Additional cell culture reagents were obtained from Gibco and HyClone. Cell fluorescence imaging was captured using a Zeiss LSM880 single-confocal laser imaging system (Germany), while animal fluorescence imaging was conducted with IVIS spectrum. Transmission electron microscopy (TEM) analyses were performed using a Thermo Scientific Talos F200S, and further material sample characterizations were carried out at the Analysis and Testing Center of Sichuan University. Particle size, polydispersity index (PDI), and surface zeta potential were measured using dynamic light scattering (DLS, Malvern Zetasizer Nano Pro). Neutron irradiation experiments were facilitated by Neuboron Medtech Ltd. (Nanjing, China).

Cells and animals

MDA-MB-231 (ATCC HTB-26), B16-F10 (ATCC CRL-6475) MCF-10A (ATCC CRL-10317), and PANC-1 cells (ATCC CRL-1469) were purchased from the American Type Culture Collection (ATCC, Rockville, USA), which were cultured in RPMI 1640 or DMEM complete medium (supplemented with 10% FBS, 1% penicillin, and 1% streptomycin) and maintained at 37 °C with humidified 5% CO₂. No authentication of these cells has been used and neither of cell lines applied in this study tested positive for Mycoplasma.

Specific pathogen-free (SPF) female nude mice (6–8 weeks) were purchased from Beijing Vital River Laboratory Animal Technologies Co., Ltd (Beijing, China). All animals were maintained at 22–23 °C, 45–55% relative humidity with a 12–12 h light-dark cycle with free food and water supplies. Findings do not apply to only one sex. Female mice were chosen due to males are aggressive to fight and usually get injured, which influences the data collection.

HPLC-MS/MS

High-performance liquid chromatography-mass spectrometry (HPLC-MS) was performed on an Agilent 1260 Infinity HPLC system equipped with a G7129A 1260 autosampler, a G7111B 1260 Quat Pump, and a G7155A 1260 DAD detector connected to a G6125B single-quadrupole

LC/MS system. H₂O (solvent A) and MeCN (solvent C), each containing 0.1% formic acid, were used as the mobile phase, and the solvent composition was controlled by a gradient program. Low-resolution mass spectra were obtained in positive ESI mode in the range 200–2000 *m/z*. HPLC traces were obtained on Agilent Eclipse plus C18 column (3 × 100 mm, 3.5 μm).

Critical aggregation concentration determination

A mixture containing Nile Red (final concentration of 1.0 μM) and a series of LA-BPA derivatives (ranging from 0 to 20 mM in final concentration) was prepared in distilled water and agitated at room temperature overnight. The fluorescence emission intensity of Nile Red at 525 nm ($\lambda_{\text{ex}} = 485$ nm) was recorded using a FluoroMax-4 fluorometer (Horiba, Kyoto, Japan). The critical aggregation concentrations of the LA-BPA derivatives in aqueous solutions were determined by identifying the intersection of two linear regressions applied to the fluorescence data.

Vesicles assembly

Prior to formation of vesicles, the pH of the LA-BPA solution was adjusted to below 7.0 using 1 M HCl, prompting the monomer to self-assemble into vesicles. Following this, the solution was titrated with 2.5 M NaOH to achieve an alkaline pH, which led to the depolymerization of the vesicles. Notably, under these conditions, the assembly-disassembly process was reversible and could be repeated.

DLS characterization

2 mg of LA-BPA derivatives were initially added to 2 mL of deionized water and sonicated for 30 s. Subsequently, an appropriate volume of 2.5 M NaOH aqueous solution was added to the mixture until the compounds completely dissolved, resulting in a fully transparent solution with a pale green color. Then, the pH of the solution was adjusted to ≤ 7.2 by the gradual addition of 1 M HCl. As the HCl was added, an emulsion formed and the color of the solution shifted from clear to slightly white. Following this, the particle size and potential of the vesicle series were analyzed using a Malvern Zetasizer Nano Pro for DLS analysis. The morphologies of the vesicles were observed using TEM after staining with 2% (w/v) phosphotungstic acid.

Coarse-graining model construction

The 3D all-atom configurations of small molecules identified as **L^pB-3** were initially constructed in both acidic and alkaline environments using the Molecular Operating Environment (MOE2020) software, and subsequently optimized at the B3LYP/6-311G* level with the Gaussian16 software to determine the stable 3D all-atom structures of the **L^pB-3** molecules in these environments. In comparison with the acidic environment, the disulfide bonds within the **L^pB-3** molecules were disrupted in the alkaline environment, accompanied by the deprotonation of the boric acid and carboxylic acid groups, as depicted in Supplementary Fig. 19. Following this, the stable 3D all-atom conformations of **L^pB-3** in both environments were coarsely grained using the auto-martini software³², resulting in the creation of stable 3D coarse-grained conformations as well as the corresponding coarse-graining force fields (bond parameters) for both environments, as illustrated in Supplementary Fig. 19.

Two initial Coarse-Graining models were constructed as depicted in Supplementary Fig. 20. One model was utilized for the aggregation simulation, while the other was applied to the deaggregation simulation. Specifically, for the aggregation simulation, the initial Coarse-Graining model was established by randomly distributing 35,000 Coarse-Graining **L^pB-3** molecules in an acidic environment and 189,000 Coarse-Graining water molecules within the simulation box. Following the aggregation simulation, this model was adapted to create the initial Coarse-Graining model for the deaggregation simulation. This adaptation involved replacing the **L^pB-3** molecules in the

acidic environment with Coarse-Graining **L^PB-3** molecules in an alkaline environment. In addition, owing to the deprotonation of the boric acid and carboxylic acid groups in the **L^PB-3** molecule under alkaline conditions, 7000 Coarse-Graining Na⁺ ions were also randomly introduced into the initial model for the deaggregation simulation to maintain electrical neutrality.

Coarse-graining simulations (aggregation simulation and deaggregation simulation)

Both Coarse-Graining simulations were performed in GROMACS (version 2021.6)³². The martini_v2.2P force field^{33,34} was used to describe the nonbond parameters of the Coarse-Graining **L^PB-3** molecules, Coarse-Graining water molecules and Coarse-Graining Na⁺ ions. Thereafter, the above produced Coarse-Graining force field from the auto-martini package³⁵ was used to describe the bond parameters of the Coarse-Graining **L^PB-3** molecules. During the MD simulations, for each Coarse-Graining model, we firstly performed a minimization step using steepest descent method to simply remove any unreasonable contacts between Coarse-Graining bonds. Then, a short equilibration step was carried out for 100 ns in a time step of 5 fs under NPT ensemble. During the equilibration phase step, the temperature was controlled by the V-rescale thermostat algorithm³⁶ with a time constant of 1.0 ps, and the pressure was controlled by the Berendsen coupling algorithm³⁷ with a time constant of 5.0 ps. Finally, a long time production phase step (about 5 μs for the Coarse-Graining model for the aggregation simulation and about 15 μs for the Coarse-Graining model for the deaggregation simulation) was carried out in a time step of 20 fs under NPT ensemble. During the production phase step, the temperature was also controlled and kept at 300 K by the V-rescale thermostat algorithm³⁶ and the pressure was also controlled and kept at 1.0 atm by the Berendsen coupling algorithm³⁷. In addition, during the whole MD simulations, the particle mesh Ewald (PME)^{38,39} method was employed to control the long-range electrostatic interactions and the cutoff value of van der Waals interaction was set as 12 Å.

The preparation and characterization of Cy5.5@vesicles

Fluorescence probe was encapsulated into vesicles following a modified solvent diffusion method, which enhances the entrapment of hydrophobic molecules within the hydrophobic layers of the vesicles. Typically, the vesicles were suspended in 5 mL of distilled water to achieve a final concentration of 5 mg/mL. The drug was diluted to a concentration of 50 mM in DMSO. Subsequently, 50 μL of the probe payload solution was added dropwise to the vesicle suspension at room temperature while vortexing, with no precipitation observed. The mixture was then transferred into a small-volume dialysis bag (MWCO = 3000 Da) and dialyzed against 1 X PBS for 24 h. The concentration of the probe in the release medium was measured by high-performance liquid chromatography (HPLC). In addition, the fluorescence emission and excitation spectra of the Cy5.5@vesicles were monitored using a HoribaMax-4 spectrofluorometer.

Cell uptake

Cellular uptake of Cy5.5@vesicles was evaluated by confocal imaging microscopy. PANC-1 cells were cultured overnight in confocal petri dishes. Subsequently, the supernatant was removed, and 2.5 mL of media containing Cy5.5@vesicles (at a final concentration of 20 μg/mL) was added to the cells, which were then incubated for 4 h at 37 °C. In the control group, the medium with Cy5.5@vesicles was replaced with fresh medium. Following the incubation period, the medium was removed, and the cells were treated with CellMask (200 nM) for 30 min, then washed three times with PBS, and finally subjected to confocal imaging.

Examination of sialic acid targeting

PANC-1 cells were plated at a density of 70–80% in 2.5-cm dishes and incubated for 24 h. Cy5.5@vesicles (200 μg mL⁻¹, with equivalent BPA

at 65 μg mL⁻¹) were administered to the cells and allowed to incubate for an additional 4 h. Concurrently, PANC-1 cells underwent pretreatment with 0.5 U of neuraminidase (to remove sialic acid residues from the surface of cancer cells) for 2 h at 37 °C before the introduction of Cy5.5@vesicles. Following a brief wash with PBS three times, the cellular uptake of Cy5.5@vesicles (200 μg mL⁻¹) was captured using confocal imaging microscopy. The human primary pancreatic acinar cells were treated with Cy5.5@vesicles under the same conditions. Fluorescent imaging was performed to examine vesicles uptake by the normal cells. The phenylboronic acids groups of vesicles were blocked with N-acetylneurameric acid (vesicles/N-acetylneurameric acid molar ratio: 1:10) for 6 h. Fluorescence intensities were quantified using Image J and normalized against the average labeling fluorescence intensity.

Synergistic anti-cancer mechanisms of L^PB-3 vesicles on PANC-1 cells

To detect intracellular GSH, PANC-1 cells were seeded at a density of 1 × 10⁵ cells per well in 6-well plates containing confocal glass culture dishes and cultured overnight. The following day, the cells were exposed to various concentrations of **L^PB-3** vesicles (0, 0.1, 0.2, 0.5 mg/mL) at 37 °C under normoxic conditions (20% O₂/5% CO₂) for 24 h. Subsequently, cellular GSH levels were determined using 5-chloromethylfluorescein diacetate (CMFDA, molecular probes), a membrane-permeable dye suitable for intracellular GSH detection. After treatment, the cells were washed three times with PBS and incubated with 5 μM CMFDA at 37 °C for 30 min. GSH depletion was further verified by confocal imaging microscopy (Excitation/Emission, 488 nm/520 nm). The fluorescence images were quantitatively analyzed using ImageJ software.

To quantify ROS in the PANC-1 cells, the cells were seeded into 6-well glass-bottom imaging plates and stimulated as previously described. Following stimulation, intracellular ROS levels were analyzed by staining the cells with 2,7-dichlorofluorescein diacetate (DCFH-DA) for 30 min in an incubator. After staining, the cells were washed with PBS and subsequently imaged using fluorescence microscopy.

To detect mitochondrial membrane potential, PANC-1 cells were treated with various concentrations of vesicles as previously described. Subsequently, the cells were incubated with a JC-1 probe (10 μg mL⁻¹) for 30 min, followed by three washes with PBS. Finally, the cells were imaged using confocal microscopy.

The preparation and characterization of Dox@vesicles

Dox was encapsulated into vesicles using a modified solvent diffusion method, designed to enhance the entrapment of hydrophobic molecules within the hydrophobic layers of the vesicles. Initially, the vesicles were suspended in 5 mL of distilled water to achieve a final concentration of 5 mg/mL. Concurrently, the Dox was diluted to a concentration of 50 mM in DMSO. A 50 μL solution containing the Dox payload was then added dropwise to the vesicle suspension at room temperature while vortexing, with no precipitation observed. Following this, the mixture was transferred into a dialysis bag (MWCO = 3000 kDa) and dialyzed against PBS for 24 h. The Dox content in the release medium was subsequently measured using high-performance liquid chromatography (HPLC).

In vitro Dox release detection

For the drug release study, 1 mL of Dox@vesicles solution at a concentration of 1 mg/mL was enclosed within a dialysis bag (MWCO: 8000–12000 Da). The encapsulated vesicles underwent dialysis against a release medium, consisting of pH 7.2 PBS and pH 7.2 PBS supplemented with 1, 2, 5, and 10 mM GSH. Sample aliquots were collected from the release medium at predetermined intervals of 0, 1, 2, 4, 6, 12, 18, 24, 36, and 48 h. Each sample withdrawn was immediately

replaced with an equal volume of pre-warmed fresh medium to maintain the volume constant throughout the experiment. The concentration of Dox in the release medium was quantitatively determined using high-performance liquid chromatography (HPLC), employing an HPLC system from Waters, America.

Efficacy assessments of Dox@vesicles in vivo

MDA-MB-231 and PANC-1 tumor-bearing nude mice were used, each bearing tumors with an average volume of ~150 mm³ for antitumor experiments. The mice received injections via the tail vein with either free Dox or Dox@vesicles at a dose of 4 mg/kg. The saline control group was administered a comparable volume of saline, while the vesicles group received an equivalent mass of **L¹⁰B-3** vesicles. No treatment was given to the control group. Each experimental group consisted of 5 mice. Tumor volumes and body weights were measured every three days, and the time-to-death for each mouse was diligently recorded.

Vesicles distribution in vivo

For the pharmacokinetic study, one group of mice ($n=3$ per group) received an injection of Cy5.5@vesicles nanoparticles (350 mg kg⁻¹, equivalent BPA 113.75 mg kg⁻¹) via the tail vein. Another group was similarly administered an equivalent dose of free fluorescent dye via the tail vein. Imaging was performed using an IVIS Spectrum in Vivo Imaging System at 1, 4, 6, and 8 h post-injection. The peak intensity distribution for the Cy5.5@vesicles at each time point was determined. Post-imaging, mice were euthanized at predetermined time points, and major organs (heart, liver, spleen, lung, kidneys) and tumors were harvested for immediate measurement of fluorescence intensity using the IVIS Spectrum. Concurrently, the boron content in these organs and tissues was quantitatively analyzed using ICP-MS. For ICP-MS analysis, the organs were digested in 5 mL of 60% nitric acid at 90 °C for 12 h, then diluted to 30 mL with deionized water and processed. Furthermore, to obtain the detailed information about the distribution of Cy5.5@vesicles within the tumor site, the mice were injected with Hoechst 33342 (5 mg kg⁻¹) and dextran-FITC (Mw: 170 kDa, 5 mg kg⁻¹) via the tail vein 6 h after Cy5.5@vesicles injection. For live-imaging experiments, the mice were anesthetized, and the tumor was exposed by a skin incision. The tumor tissues were visualized by upright single-photon confocal microscopy (Nikon A1R+MP, Japan).

Efficacy assessments of BNCT on PANC-1 cells

All cell or animal irradiation experiments were conducted at the Xiamen Humanity Hospital-Neuboron BNCT Center, utilizing the Neu-PexTM Block-I AB-BNCT system. Initially, 5×10^6 PANC-1 cells were seeded into 10-cm dishes, allowed to adhere over 24 h, and subsequently incubated with varying concentrations (0, 500, 1000 µg mL⁻¹) of vesicles for 6 h at 37 °C. For groups receiving combined BNCT and chemotherapy, post-neutron irradiation, cells were treated with Dox@vesicles for an additional 6 h. Cells were then rinsed with PBS, harvested via trypsinization, and washed thrice using RPMI 1640 supplemented with 10% FBS. Prior to neutron irradiation, cells treated with different vesicle dosages were resuspended in 1 mL of culture medium and transferred to 1.5 mL Eppendorf tubes, which were then secured in the designated holder. The holder was placed in the irradiation port for neutron exposure for 10 min, with an epithermal neutron flux of 8.015×10^8 n/cm²/s. Post-irradiation, cells were cultured for secondary evaluation of efficacy. To assess apoptosis on the second day, apoptotic cells were identified using a TUNEL assay (per manufacturer's instructions) and quantified via flow cytometry. Concurrently, for the calcein-AM/propidium iodide (calcein-AM/PI) assay, cells were processed as previously described, with calcein-AM/PI stock solutions prepared in culture medium to final concentrations of 2 µM calcein-AM and 4.5 µM PI, followed by observation using confocal fluorescence microscopy.

For γ-H2AX staining, cells were first washed with PBS three times and then fixed with 4% paraformaldehyde for 10 min at room temperature. Following another PBS wash, the cells were incubated with 5% FBS for 30 min and treated with 0.3% Triton X-100 in PBS for 10 min at room temperature. After aspirating the supernatant, the rabbit anti-rat γ-H2AX primary antibody (CST, 50 µL, 1:200) was added, and the cells were incubated for 2 h at 37 °C. Subsequently, the cells were washed with PBS and incubated with goat anti-rabbit Alexa Fluor 647 secondary antibody (CST, 50 µL, 1:1000) for 1 h at 37 °C. Nuclei were stained with Hoechst 33342 (5 µM), followed by a brief wash with PBS. Finally, images were captured using a Zeiss 880 laser scanning microscope.

Evaluation of antitumor efficiency on subcutaneous PANC-1 tumor bearing mice

To assess tumor growth in vivo, subcutaneous pancreatic cancer models were established using PANC-1 cells. Nude mice were inoculated with 1×10^6 PANC-1 cells per mouse, suspended in a PBS and Matrigel solution at a 1:1 volume ratio. Once the tumor volume reached ~120 mm³. The nude tumor-bearing mice were randomly divided into six groups, with eight mice per group. Tumor volume (mm³) was calculated according to the following formula: tumor volume = 0.5 × length × width². Animals were grouped as following: normal control group, a neutron irradiated control group, a low-dose **L¹⁰B-3** vesicles group with neutron irradiation (250 mg/kg), a low-dose Dox@vesicles group with neutron irradiation (250 mg/kg **L¹⁰B-3** vesicles and 5 mg/kg Dox), a low-dose Dox@vesicles group without irradiation, a high-dose vesicles group with neutron irradiation (350 mg/kg), and a high-dose vesicles group without irradiation. In the control groups, mice were injected with an equivalent volume of saline. Six hours post-neutron irradiation, the animals were lightly anesthetized with isoflurane, followed by deep anesthesia using intraperitoneal sodium pentobarbital. Mice were then secured in a holder, which was placed into the irradiation port for a duration of 9 to 14 min. After irradiation, mice were returned to their home cages and allowed to recover, with free access to water and food. Throughout the four-week treatment period, tumor volume was measured every other day using digital vernier calipers, and body weight was monitored for potential changes. Natural survival rates were documented. At the end of the experiment, major organs (the heart, liver, spleen, lung, and kidney) were collected for pathological analysis. These organs were embedded in paraffin, sectioned into approximately 5-µm slices, and stained with hematoxylin and eosin (H&E) for histological examination under light microscopy. Tumor tissues were also processed for H&E, TUNEL, and Ki67 staining, with eight randomly selected sections quantified per animal.

The in vivo antitumor efficacy evaluated on melanoma models

To evaluate the efficacy of **L¹⁰B-3** vesicles as BNCT agents against tumor, we used an orthotopic B16F010 melanoma model, an immune model. C57 mice were inoculated with 1×10^6 B16F10 cells per mouse, suspended in a PBS. Once the tumor volume reached ~100 mm³. The melanoma tumor bearing mice were randomly divided into four groups, with eight mice per group. Tumor volume (mm³) was calculated according to the following formula: tumor volume = 0.5 × length × width². Animals were grouped as following: normal control group, a neutron irradiated control group, **L¹⁰B-3** vesicles group (350 mg/kg) with neutron irradiation and **L¹⁰B-3** vesicles group (350 mg/kg) without neutron irradiation. Throughout the experimental period, tumor volume was measured every other day using digital vernier calipers, and body weight was monitored for potential changes. Natural survival rates were documented. At the end of the experiment, major organs (the heart, liver, spleen, lung, and kidney) and tumor tissues were collected for pathological analysis.

Radiation dose calculation for the in vitro and in vivo experiments involved irradiating cells and mice using the accelerator-based BNCT

system, NeuPex, developed by Neuboron Therapy System Ltd., Xiamen, China (<https://en.neuboron.com/products>). This system operates at a neutron accelerator voltage of 2.3 MeV and a current of 7 mA. During irradiation, the cells or mice were securely placed in their respective holders, which were then positioned within the irradiation port. Both the cell holder and the mouse holding device were meticulously engineered to ensure a uniform, low-contamination, and high-intensity thermal neutron field reached the targets.

To accurately estimate the received dose, the experiments involving mice and cells were meticulously modeled and computed using the Monte Carlo method. Radiation doses were determined utilizing the Monte Carlo toolkit PHITS (ver. 3.16) in conjunction with the ENDF/B-VIII.0 cross-section library. The computational model encompassed the neutron source, beam shaping assembly, irradiation port, and the device subjecting the cells/mice to irradiation. The neutron beam model was crafted according to an elaborate geometric description of the NeuPex AB-BNCT system. A cell model consisted of a uniform layer measuring 10 µm in thickness. The mouse model was developed using a voxel model paired with the lattice tally method, incorporating organ at risk (OAR) data derived from actual CT images. Information on elemental composition and density from ICRU 46 was also incorporated. The treatment planning system NeuMANTA (Neuboron Multi-functional Arithmetic for Neutron Transportation Analysis) was employed for ROI contouring. The boron dose was computed based on boron concentration measurements from biological samples, as detailed in other sections. Based on this, the physical dose components for the cells or mice were calculated.

Statistical analysis

All slices were analyzed using ImageJ, and all data are expressed as the mean ± standard deviation. For two groups, a Student's *t*-test was conducted, while an analysis of variance (ANOVA) was utilized for multiple groups. Differences were considered significant if the *p*-value was less than 0.05. The statistical analyses were carried out using GraphPad Prism 7.0.

Reporting summary

Further information on research design is available in the Nature Portfolio Reporting Summary linked to this article.

Data availability

General synthesis procedure of LA-BPA derivatives as well as the NMR analysis characterizing LA-BPA derivatives are summarized in Supplementary Note 2 of Supplementary information file. Mass spectrometry data of L³B-3 is included in Supplementary Fig. 5a and source data file. All other data supporting the findings in this study are available in the main text, supplementary information or source data file. Source data are provided with this paper.

References

1. Mitchell, M. J. et al. Engineering precision nanoparticles for drug delivery. *Nat. Rev. Drug Discov.* **20**, 101–124 (2021).
2. Izci, M., Maksoudian, C., Manshian, B. B. & Soenen, S. J. The use of alternative strategies for enhanced nanoparticle delivery to solid tumors. *Chem. Rev.* **121**, 1746–1803 (2021).
3. Wang, D. et al. Nucleoside analogue-based supramolecular nano-drugs driven by molecular recognition for synergistic cancer therapy. *J. Am. Chem. Soc.* **140**, 8797–8806 (2018).
4. Matsumura, Y. & Maeda, H. A new concept for macromolecular therapeutics in cancer chemotherapy: mechanism of tumoritropic accumulation of proteins and the antitumor agent smancs. *Cancer Res.* **46**, 6387–6392 (1986).
5. Anselmo, A. C. & Mitragotri, S. Nanoparticles in the clinic: an update. *Bioeng. Transl. Med.* **4**, e10143 (2019).
6. Baek, M.-J. et al. Tailoring renal-clearable zwitterionic cyclodextrin for colorectal cancer-selective drug delivery. *Nat. Nanotechnol.* **18**, 945–956 (2023).
7. Liu, H. et al. Dual-responsive surfaces modified with phenylboronic acid-containing polymer brush to reversibly capture and release cancer cells. *J. Am. Chem. Soc.* **135**, 7603–7609 (2013).
8. Stabelius, A., Lee, S. & Almutairi, A. The chemistry of boronic acids in nanomaterials for drug delivery. *Acc. Chem. Res.* **52**, 3108–3119 (2019).
9. Wang, R. et al. Phenylboronic acid modification augments the lysosome escape and antitumor efficacy of a cylindrical polymer brush-based prodrug. *J. Am. Chem. Soc.* **143**, 20927–20938 (2021).
10. Liu, Y., Jia, Y., Wu, Q. & Moore, J. S. Architecture-controlled ring-opening polymerization for dynamic covalent poly(disulfide)s. *J. Am. Chem. Soc.* **141**, 17075–17080 (2019).
11. Zhang, X. & Waymouth, R. M. 1,2-dithiolane-derived dynamic, covalent materials: cooperative self-assembly and reversible cross-linking. *J. Am. Chem. Soc.* **139**, 3822–3833 (2017).
12. Deng, Y. et al. Acylhydrazine-based reticular hydrogen bonds enable robust, tough, and dynamic supramolecular materials. *Sci. Adv.* **8**, eabk3286 (2022).
13. Wang, B.-S. et al. Acid-catalyzed disulfide-mediated reversible polymerization for recyclable dynamic covalent materials. *Angew. Chem., Int. Ed.* **62**, e202215329 (2023).
14. Zhang, Q., Qu, D.-H., Feringa, B. L. & Tian, H. Disulfide-mediated reversible polymerization toward intrinsically dynamic smart materials. *J. Am. Chem. Soc.* **144**, 2022–2033 (2022).
15. Jiang, C.-S., Mueller, W. E. G., Schroeder, H. C. & Guo, Y.-W. Disulfide- and multisulfide-containing metabolites from marine organisms. *Chem. Rev.* **112**, 2179–2207 (2012).
16. Yang, Y. & Urban, M. W. Self-healing polymeric materials. *Chem. Soc. Rev.* **42**, 7446–7467 (2013).
17. Barcan, G. A., Zhang, X. & Waymouth, R. M. Structurally dynamic hydrogels derived from 1,2-dithiolanes. *J. Am. Chem. Soc.* **137**, 5650–5653 (2015).
18. Qin, X. et al. Rational design of nanocarriers for intracellular protein delivery. *Adv. Mater.* **31**, 1902791 (2019).
19. Zhang, Q. et al. Dual closed-loop chemical recycling of synthetic polymers by intrinsically reconfigurable poly(disulfides). *Matter* **4**, 1352–1364 (2021).
20. Li, S. et al. A hierarchical coding strategy for live cell imaging of protein-specific glycoform. *Angew. Chem., Int. Ed.* **57**, 12007–12011 (2018).
21. Chan, L. et al. Sequentially triggered delivery system of black phosphorus quantum dots with surface charge-switching ability for precise tumor radiosensitization. *ACS NANO* **12**, 12401–12415 (2018).
22. Zhao, Z. M., Ukidve, A., Kim, J. & Mitragotri, S. Targeting strategies for tissue-specific drug delivery. *Cell* **181**, 151–167 (2020).
23. Peng, X.-X. et al. Gallium triggers ferroptosis through a synergistic mechanism. *Angew. Chem., Int. Ed.* **62**, e202307838 (2023).
24. Ke, L. et al. A biodegradable iridium(III) coordination polymer for enhanced two-photon photodynamic therapy using an apoptosis-ferroptosis hybrid pathway. *Angew. Chem., Int. Ed.* **61**, e202205429 (2022).
25. Li, F. et al. Spatiotemporally programmable cascade hybridization of hairpin DNA in polymeric nanoframework for precise siRNA delivery. *Nat. Commun.* **12**, 1138 (2021).
26. Pereira, D. B. et al. Fluorescent false neurotransmitter reveals functionally silent dopamine vesicle clusters in the striatum. *Nat. Neurosci.* **19**, 578–586 (2016).
27. Shi, Y. et al. Tracing boron with fluorescence and positron emission tomography imaging of boronated porphyrin nanocomplex for imaging-guided boron neutron capture therapy. *ACS Appl. Mater. Interfaces* **10**, 43387–43395 (2018).

28. Zhu, Y. et al. Tamoxifen-resistant breast cancer cells are resistant to DNA-damaging chemotherapy because of upregulated BARD1 and BRCA1. *Nat. Commun.* **9**, 1595 (2018).
29. Nomoto, T. et al. Poly(vinyl alcohol) boosting therapeutic potential of *p*-boronophenylalanine in neutron capture therapy by modulating metabolism. *Sci. Adv.* **6**, eaaz1722 (2020).
30. Li, J. et al. Boron encapsulated in a liposome can be used for combinational neutron capture therapy. *Nat. Commun.* **13**, 2143 (2022).
31. Kuthala, N., Vankayala, R., Li, Y.-N., Chiang, C.-S. & Hwang, K. C. Engineering novel targeted boron-10-enriched theranostic nanomedicine to combat against murine brain tumors via MR imaging-guided boron neutron capture therapy. *Adv. Mater.* **29**, 1700850 (2017).
32. Abraham, M. J. et al. Gromacs: High performance molecular simulations through multi-level parallelism from laptops to supercomputers. *SoftwareX* **1-2**, 19–25 (2015).
33. de Jong, D. H. et al. Improved parameters for the martini coarse-grained protein force field. *J. Chem. Theory Comput.* **9**, 687–697 (2013).
34. Vuorela, T. et al. Role of lipids in spheroidal high density lipoproteins. *PLoS Comput. Biol.* **6**, e1000964 (2010).
35. Bereau, T. & Kremer, K. Automated parametrization of the coarse-grained martini force field for small organic molecules. *J. Chem. Theory Comput.* **11**, 2783–2791 (2015).
36. Bussi, G., Donadio, D. & Parrinello, M. Canonical sampling through velocity rescaling. *J. Chem. Phys.* **126**, 014101 (2007).
37. Berendsen, H. J. C., Postma, J. P. M., Vangunsteren, W. F., Dinola, A. & Haak, J. R. Molecular-dynamics with coupling to an external bath. *J. Chem. Phys.* **81**, 3684–3690 (1984).
38. Darden, T., York, D. & Pedersen, L. Particle mesh Ewald—an n.Log(n) method for Ewald sums in large systems. *J. Chem. Phys.* **98**, 10089–10092 (1993).
39. Essmann, U. et al. A smooth particle mesh Ewald method. *J. Chem. Phys.* **103**, 8577–8593 (1995).

Acknowledgements

The authors thank Feijing Su Core Facilities of West China Hospital for NMR tests. We also greatly appreciate the help of Dr. Shanling Wang from the Analytical & Testing Center at Sichuan University for the TEM analysis of our nanoparticles. This work was financially supported by the National Natural Science Foundation of China (U21A20417), the Sichuan Science and Technology Program (2022YFS0333), the Fundamental Research Funds for the Central Universities (20826041F4138) and 1-3-5 project for disciplines of excellence, West China Hospital, Sichuan University (ZYGD18002).

Author contributions

L.D. conceived the work, performed the experiments, analyzed the data, and wrote the paper. J.L., X.Y., and L.P. contributed to the L⁹B-3 vesicles characterization and flow cytometry assays. T.Y., Y.L., S.Z., D.S., and Y.L. contributed to the animal experiments. W.M. and Z.Q. conceived and supervised the project and wrote the paper.

Competing interests

The authors declare no competing interests.

Additional information

Supplementary information The online version contains supplementary material available at <https://doi.org/10.1038/s41467-025-56507-4>.

Correspondence and requests for materials should be addressed to Wuyu Mao or Zhiyong Qian.

Peer review information *Nature Communications* thanks Ferdinando Pucci, and the other, anonymous, reviewer(s) for their contribution to the peer review of this work. A peer review file is available.

Reprints and permissions information is available at <http://www.nature.com/reprints>

Publisher's note Springer Nature remains neutral with regard to jurisdictional claims in published maps and institutional affiliations.

Open Access This article is licensed under a Creative Commons Attribution-NonCommercial-NoDerivatives 4.0 International License, which permits any non-commercial use, sharing, distribution and reproduction in any medium or format, as long as you give appropriate credit to the original author(s) and the source, provide a link to the Creative Commons licence, and indicate if you modified the licensed material. You do not have permission under this licence to share adapted material derived from this article or parts of it. The images or other third party material in this article are included in the article's Creative Commons licence, unless indicated otherwise in a credit line to the material. If material is not included in the article's Creative Commons licence and your intended use is not permitted by statutory regulation or exceeds the permitted use, you will need to obtain permission directly from the copyright holder. To view a copy of this licence, visit <http://creativecommons.org/licenses/by-nc-nd/4.0/>.

© The Author(s) 2025